

## RESEARCH ARTICLE

# Oncogenic gain of function due to p53 amyloids occurs through aberrant alteration of cell cycle and proliferation

Ambuja Navalkar<sup>1</sup>, Ajoy Paul<sup>1</sup>, Arunima Sakunthala<sup>1</sup>, Satyaprakash Pandey<sup>1</sup>, Amit Kumar Dey<sup>2</sup>, Sandhini Saha<sup>2</sup>, Sarthak Sahoo<sup>3</sup>, Mohit Kumar Jolly<sup>3</sup>, Tushar K. Maiti<sup>2</sup> and Samir K. Maji<sup>1,\*</sup>

## ABSTRACT

Transcription factor p53 (also known as TP53) has been shown to aggregate into cytoplasmic and nuclear inclusions, compromising its native tumor suppressive functions. Recently, p53 has been shown to form amyloids, which play a role in conferring cancerous properties to cells, leading to tumorigenesis. However, the exact pathways involved in p53 amyloid-mediated cellular transformations are unknown. Here, using an *in cellulo* model of full-length p53 amyloid formation, we demonstrate the mechanism of loss of p53 tumor-suppressive function with concomitant oncogenic gain of functions. Global gene expression profiling of cells suggests that p53 amyloid formation dysregulates genes associated with the cell cycle, proliferation, apoptosis and senescence along with major signaling pathways. This is further supported by a proteome analysis, showing a significant alteration in levels of p53 target proteins and enhanced metabolism, which enables the survival of cells. Our data indicate that specifically targeting the key molecules in pathways affected by p53 amyloid formation, such as cyclin-dependent kinase-1, leads to loss of the oncogenic phenotype and induces apoptosis of cells. Overall, our work establishes the mechanism of the transformation of cells due to p53 amyloids leading to cancer pathogenesis.

This article has an associated First Person interview with the first author of the paper.

**KEY WORDS:** p53 amyloids, Cancer, Tumor suppression, Oncogenic gain-of-function

## INTRODUCTION


p53 (also known as TP53) is a tumor suppressor protein involved in the regulation of key cellular processes like apoptosis, cell cycle arrest, cell proliferation and DNA damage repair (Fuster et al., 2007; Zilfou and Lowe, 2009). Cancer-associated p53 mutations have been shown to be associated with loss of the p53 tumor suppressive functions and concomitant gain of oncogenic functions (Muller and Vousden, 2013; Oren and Rotter, 2010). p53 mutations most often increase the half-life of the protein, leading to it forming inclusions

containing p53 aggregates in the nucleus as well as the cytoplasm (De Smet et al., 2017; Moll et al., 1996; Ostermeyer et al., 1996). The aggregation and cytoplasmic sequestration of wild-type p53 is also detected in a subset of primary human tumors, such as breast cancer, colon cancer and neuroblastoma (NB) (Bosari et al., 1994, 1995; Moll et al., 1995, 1992). A study on p53 aggregation using six human cancer tissues linked the poor clinical outcome of tumors with p53 aggregation (De Smet et al., 2017). Likewise, p53 aggregation has also been detected in astrocytoma and osteosarcoma, along with bladder, colon and pharynx carcinoma (Xu et al., 2011). Indeed, the p53 protein contains unstructured regions and an aggregation-prone sequence (Bell et al., 2002; Ghosh et al., 2014), which might promote the destabilization and aggregation of the p53 in cancer cells (Ano Bom et al., 2012; Rangel et al., 2014; Silva et al., 2018, 2014). Based on the observation that different domains of p53 can form amyloid aggregates *in vitro* (Wang and Fersht, 2012, 2015, 2017; Wilcken et al., 2012), it is hypothesized that p53 amyloid formation is associated with p53 loss of function in cancers. Various cancer tissues as well as cancer cells have been shown to contain p53 amyloids, further supporting the link between p53 amyloids and cancer pathogenesis (Ano Bom et al., 2012; Xu et al., 2011). Additionally, our group established the presence of p53 amyloid aggregates in human breast and lung cancer tissues (Ghosh et al., 2017). Also, p53 mutation (R175H) destabilizes the p53 core domain and aggravates the amyloid fibril formation (Ghosh et al., 2017). p53 amyloid fibrils also show cell-to-cell transmission capacity suggesting that the p53 amyloid has a prion-like property (Ghosh et al., 2017).

To conclusively link p53 amyloid formation with cancer causation, we have recently demonstrated that p53 amyloid formation can enhance the oncogenic traits in non-cancerous cells (Ghosh et al., 2017; Navalkar et al., 2021). Induction of amyloid formation of wild-type p53 has been shown to contribute to the gain of oncogenic phenotypes like high proliferative and migratory potential, and also lead to resistance against drug-induced apoptosis (Navalkar et al., 2021). Considering the evidence that p53 amyloids contribute to cell survival as opposed to cell death/apoptosis (Navalkar et al., 2021), we hypothesized that this gain of function might be a consequence of alterations in several cellular pathways. To analyze this, here, we performed microarray analysis and proteomic profiling of cells containing p53 amyloids. To do this, we used our inducible cell model of p53 amyloid aggregation (Ghosh et al., 2017; Navalkar et al., 2021) to evaluate the cellular changes associated with p53 amyloid formation. Cells were treated exogenously with amyloid seeds of the p53 core DNA-binding domain (p53 94–312). The cells were analyzed immediately after fibril treatment and after passaging to understand how p53 amyloid formation changes signaling pathways. Our data suggest that apart from signaling cascades involving cell cycle and proliferation, those for apoptosis, DNA repair, chromatin organization, cell migration, metabolism and senescence are also significantly altered due to p53

<sup>1</sup>Department of Biosciences and Bioengineering, Indian Institute of Technology Bombay, Powai, Mumbai 400076, India. <sup>2</sup>Functional Proteomics Laboratory, Regional Centre for Biotechnology, Faridabad 121001, India. <sup>3</sup>Centre for BioSystems Science and Engineering (BSSE), Indian Institute of Science, Bengaluru 560012, India.

\*Author for correspondence (samirmaji@iitb.ac.in)

 A.N., 0000-0002-7407-442X; A.P., 0000-0003-4063-5919; A.S., 0000-0001-7483-6327; S.P., 0000-0001-9541-6567; A.K.D., 0000-0003-3106-7091; M.K.J., 0000-0002-6631-2109; T.K.M., 0000-0003-4721-827X; S.K.M., 0000-0002-9110-1565

Handling Editor: John Heath  
Received 26 October 2021; Accepted 4 July 2022

amyloid formation. All these changes in the cellular pathways favor cell survival even in stress conditions. This is further supported by the downregulation of tumor suppressive genes and upregulation of chaperone machinery and the unfolded protein response (UPR) in cells with p53 amyloids.

Furthermore, the fibril-treated cells show an upregulation of metabolic pathways along with an increase in expression of oncogenes, which was more prominent in the later passages, suggesting a progressive gain of oncogenic function in cells with p53 amyloids. Additionally, the comparison of microarray data for different mutants in cells with p53 amyloid suggests that p53 amyloids contribute aggressively to the loss and gain of the tumor suppressive function of p53. Further, treatment with chemical inhibitors or siRNAs directed against key players [for example, cyclin-dependent kinases (CDKs) and mitogen activated protein kinases (MAPKs)] of amyloid-mediated transformation reduced the oncogenic addiction of cells, thereby decreasing the cancerous hyperproliferation, confirming the pathways by which p53 amyloid-mediated cancerous transformation occurs. The present data will help to establish the mechanisms of p53 amyloid-mediated cancer pathogenesis.

## RESULTS

### p53 amyloid formation in cells leads to a progressive gain of oncogenic traits

Amyloid seeds of the p53 core domain can readily internalize upon exogenous addition in the cells and template the native p53 to form amyloid aggregates (Ghosh et al., 2017; Navalkar et al., 2021). p53 amyloids thus formed can transmit through cell generations and enable tumor formation when these cells are xenografted in mice (Navalkar et al., 2021). We hypothesized that p53 aggregation and amyloid formation results in widespread changes in the cellular pathways, which enhance the oncogenic traits in cells over generations. To demonstrate this, we exogenously added *in vitro* prepared sonicated p53 core amyloid seeds to the MCF 10A cells (Fig. 1A; Fig. S1A–C). The cells were further passaged continuously as per the established protocol (Navalkar et al., 2021) without any consequent addition of fibrils. Each passage was termed as T1, T2 and so on (Fig. 1B). To study how these cells acquire oncogenic properties at the early stage and the later cell generations, we first compared the cellular property at the early (T1) and late passages (T5) of cells (Fig. 1B) containing p53 amyloids. p53 core fibril treatment leads to the formation of intracellular p53 amyloid fibrils (detected as aggregates positive for staining by the amyloid-specific antibody OC; Kaye et al., 2007) at the first passage (T1), predominately in the nucleus of MCF 10A cells (Fig. 1C). The p53 aggregates persist at the T5 passage with a significant increase in p53 accumulation during passaging (Fig. 1C; Fig. S1D). This is further consistent with the fact that p53 at the T5 passage was detected in the insoluble fraction of the cell lysates (Fig. S1E). The presence of p53 amyloids allows cells to acquire a survival advantage as evident by cell death analysis using flow cytometry. The T5 passage cells showed enhanced survival in comparison to the corresponding untreated control (Fig. 1D). Cells at T5 showed lower expression of senescence marker [senescence-associated  $\beta$ -galactosidase (SA- $\beta$ -gal); Gary and Kindell, 2005] (Fig. 1E; Fig. S1F) as well as a higher colony formation potential in a soft agar colony formation assay, compared to p53 amyloid-containing T1 stage cells (Fig. 1F; Fig. S1G,H).

Furthermore, MCF 10A cells were treated with core monomer and  $\alpha$ -synuclein fibrils as a control (Fig. 2A). These cells do not show aggregation and amyloid formation by full-length endogenous p53 as analyzed by immunostaining with the anti-p53 DO-1

antibody (recognizing residues 11–25 in the native p53), the PAb240 antibody (specific to misfolded p53; Parrales et al., 2016) and the amyloid-specific OC antibody (Fig. 2A; Fig. S2A,B). The soft agar colony formation assay and proliferative population of cells (estimated with Ki-67 staining) further showed negligible changes to the cellular phenotype due to core monomer and  $\alpha$ -synuclein fibril treatment (Fig. 2B; Fig. S2C–E). However, an increase in Ki-67-positive cells has been previously reported for core fibril treatment of these cells (Navalkar et al., 2021). This indicates that p53 amyloid formation and consequent cellular changes are specific to treatment with p53 amyloid seeds.

To validate that the endogenous host p53 amyloid formation is essential for enhanced transformation potential, we used p53-null Saos-2 osteosarcoma cells treated with p53 core monomeric protein and core fibrils (Fig. 2C; Fig. S3A). The internalization of p53 core fibrils in Saos-2 cells was confirmed using FITC-labeled core fibrils (Fig. S3B). Furthermore, we examined p53 status by immunostaining the core fibril-treated Saos-2 cells with the p53 DO-1, OC and PAb240 antibodies (Fig. 2C; Fig. S3A–C). Interestingly the cells do not show any p53 stabilization or aggregation, which must be due to the lack of endogenous full-length p53 (Fig. 2C; Fig. S3A–C).  $\alpha$ -Synuclein fibril treatment also had no effect on p53 status in these cells (Fig. S3D). Given that no p53 amyloid formation was induced, no enhancement of oncogenic properties (proliferative or transformative) was seen in these cells (Fig. 2D,E; Fig. S3E–G). We further evaluated the gene expression levels using quantitative real-time PCR (qRT-PCR) for p53-linked genes [p21 (*CDKN1A*), *BAX* and *MAPK1*] in the core monomer- or  $\alpha$ -synuclein fibril-treated MCF 10A cells as well as core fibril-treated Saos-2 cells as compared to the corresponding untreated cells. No significant alteration in expression of these genes (low fold change values) was observed for all these treatments (Fig. 2F).

Taken together, these results indicate that the presence of p53 amyloid aggregates confers transformative potential to the cells, which is enhanced as the cells are passaged. The progression of a normal cell toward a cancerous one is often accompanied by multiple steps of dysregulations in the cellular pathways that confer selective advantages upon the altered cells (Sever and Brugge, 2015). We analyzed these changes using a system-level study (genomic and proteomic level) in fibril-treated cells containing p53 amyloids at T1 and T5.

### Gene expression changes due to p53 amyloid formation show alterations in cell cycle and proliferative pathways

Cancer is a multifaceted disease often needing a complexity of changes to propel a normal cell to malignancy and eventually leading to a metastatic phenotype (Hanahan and Weinberg, 2000). Specific perturbations in gene expression patterns have been implicated in the initiation and progression of cancer (Macaluso et al., 2003). We hypothesized that p53 amyloid-mediated transformation is governed by such sequential alterations in the cellular pathways. To understand the immediate effect of p53 amyloid formation and its eventual consequences, we performed a global gene expression analysis of MCF 10A cells with p53 amyloids at two different generations – the initial (T1) and later (T5) generation – by performing a microarray analysis (Fig. 3A). Bioinformatic analysis revealed 2160 transcripts (at T1) and 1008 transcripts (at T5) were differentially regulated upon core fibril treatment as compared to the untreated control. 425 genes were seen to overlap between T1 (19% of 2484 transcripts) and T5 (42% of 1112 transcripts) highlighting the central role of p53 in regulating gene expression (Fig. 3B,C). The higher number of genes influenced at T1, compared to T5, suggests that exogenous addition of p53 core

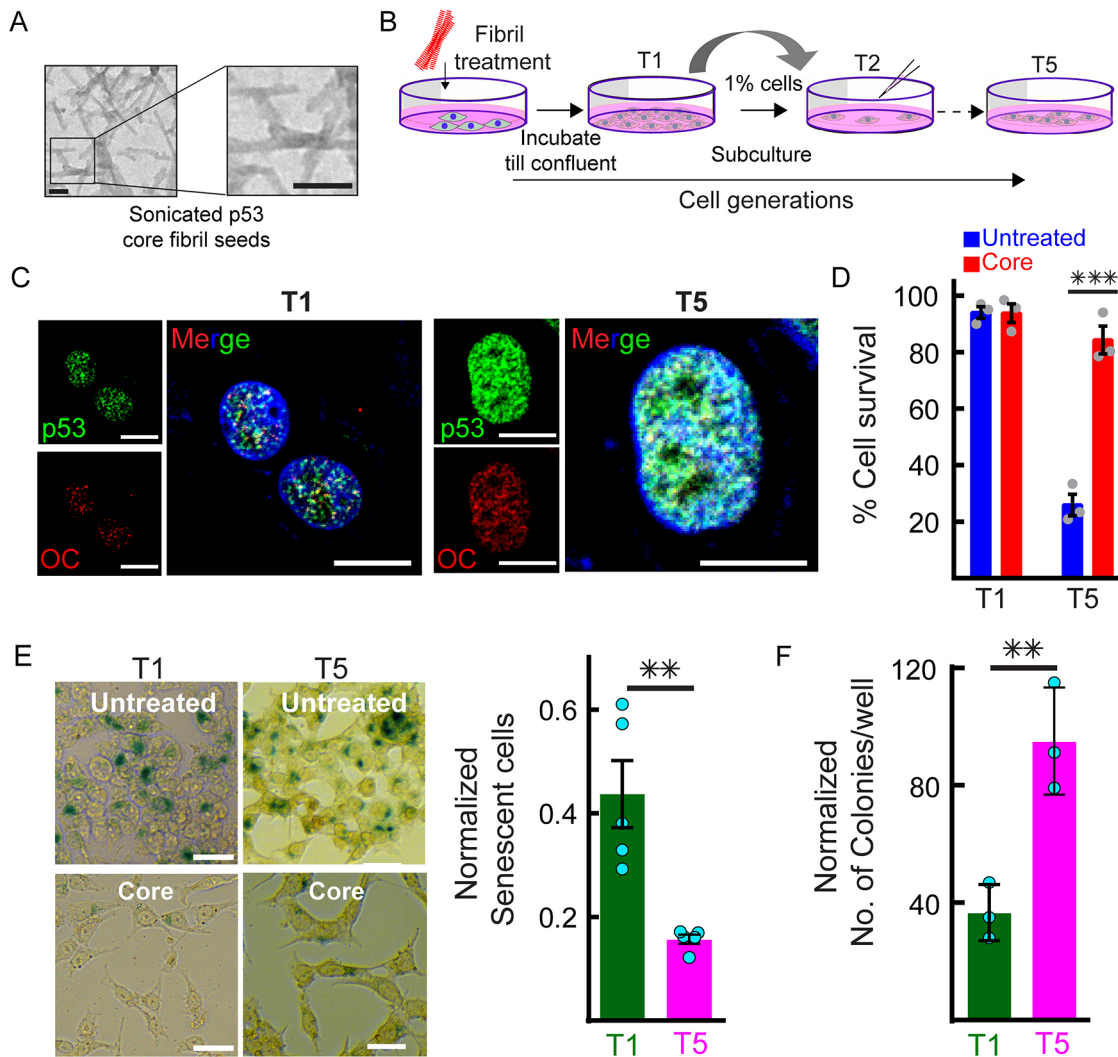


**Fig. 1. Loss of function and gain of oncogenic function upon p53 amyloid formation in cells at two different stages.** (A) Representative transmission electron micrograph (TEM) of sonicated p53 core domain amyloid fibrils aggregated in the presence of chondroitin sulphate A (CSA). Images representative of  $n=3$  independent experiments. Scale bars: 500 nm. (B) Schematic showing generation of cells containing p53 amyloids. Each cell generation after fibril treatment was labeled as T1, T2 and so on. Initial passage T1 and later passage T5 were analyzed further to evaluate the changes in cells due to amyloid formation. (C) Immunostaining of p53 core fibril-treated cells with anti-p53 antibody and the amyloid-specific antibody OC, over the passages. Colocalization of p53 and amyloid staining (OC) at two different stages of cells showing a higher amount of p53 aggregates and amyloids at T5 compared to the T1 stage. Images representative of  $n=3$  independent experiments. Scale bars: 10 μm. (D) Annexin-V-FITC/PI assay coupled with FACS analysis showing higher cell survival due to p53 amyloid at the T5 stage. Untreated cells show significantly decreased viability at the higher passage T5 as compared to the fibril-treated cells at T5. The values in the plots represent mean $\pm$ s.e.m.,  $n=3$  independent experiments. The  $P$ -value for the T5 passage (untreated vs core treated) is 0.00071 (\*\*\*). (E) Cells containing p53 amyloids at T1 and T5 showing resistance to cellular senescence quantified using X-gal assay for detection of senescence-associated biomarker  $\beta$ -galactosidase. Results are mean $\pm$ s.e.m. ( $n=3$ ). Scale bars: 40 μm. The  $P$ -value for T1 and T5 comparison is 0.00271 (\*\*). (F) Soft agar colony formation assay demonstrating that cells treated with core fibrils have significantly transformative potential as compared to the untreated control at T1 and T5 passage. The colony number was normalized with corresponding untreated cells at T1 and T5. Furthermore, at the T5 passage, the cells have a higher colony formation propensity as compared to T1 passage fibril treated cells, suggesting that p53 amyloid formation in cells leads to enhancement of transforming properties. The values were plotted as mean $\pm$ s.e.m.,  $n=3$  independent experiments. The  $P$ -value for T1 and T5 comparison is 0.05081 (\*\*). Statistical significance was calculated by one-way ANOVA followed by Bonferroni multiple comparison post-hoc test with a 95% confidence interval.

amyloid seeds and subsequent p53 amyloid formation in cells immediately deregulates many cellular pathways (at the beginning), contributing to the survival of cells. Significantly affected genes in both T1 and T5 were annotated in terms of biological processes, cellular components and molecular function (Fig. S4A,B). We further performed a pathway enrichment analysis to examine the cellular response upon loss of p53 function exclusively due to p53 aggregation, using Metascape (Zhou et al., 2019b). Metascape analysis shows pathways that are significantly affected by p53 amyloid formation at T1 and T5 generations, respectively (Fig. 3D,

E). At the T1 generation, cell cycle, apoptosis and DNA repair are significantly perturbed. Similarly, the T5 generation also showed perturbation of pathways involved in the cell cycle, DNA replication, cell migration and cell division (Fig. 3E).

Furthermore, at the T1 passage, *CDC6*, *CDK4*, *CDC45*, *PCNA*, *E2F2*, *RAD51* and *TIMELESS* genes, which are involved in cell cycle checkpoints, senescence and DNA repair processes, were downregulated, suggesting the loss of p53 tumor suppressive network (loss of native p53 regulatory control). Also, the pro-apoptotic genes (e.g. *DAPK3*) and genes involved in proofreading

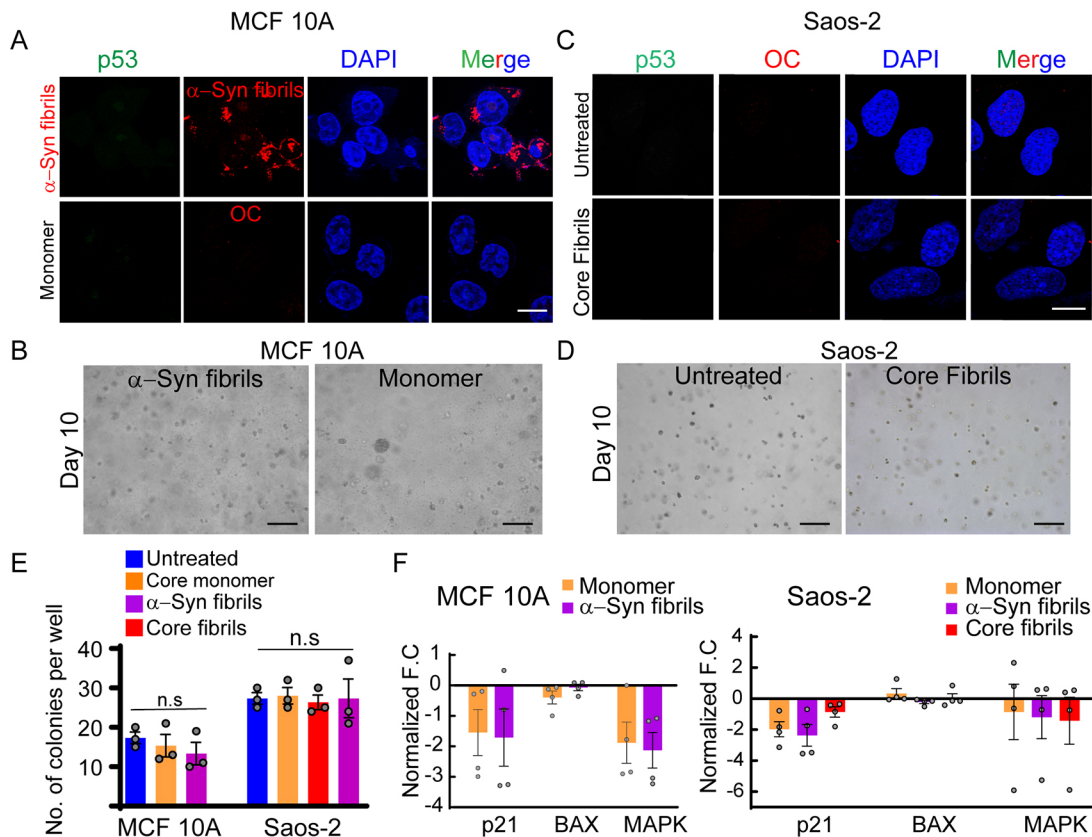


**Fig. 2. Evaluation of cellular status in MCF 10A cells treated with p53 monomers,  $\alpha$ -synuclein fibrils and Saos-2 cells treated with p53 core fibrils.** (A) Immunofluorescence analysis of MCF 10A cells treated with  $\alpha$ -synuclein ( $\alpha$ -Syn) fibril seeds (upper panel) and monomeric core protein (no amyloid, lower panel) for 48 h showing no p53 stabilization. The monomer-treated cells also did not show amyloid specific OC signal (lower panel). The data indicate that p53 amyloid formation in MCF 10A cannot be induced by monomeric p53 core domain or  $\alpha$ -synuclein fibril seeds and is specific to the addition of p53 core fibril seeds. Scale bar: 10  $\mu$ m. (B) Soft agar colony formation assay using MCF 10A cells treated with p53 core monomers or  $\alpha$ -synuclein fibril seeds showing negligible colony formation in 10 days as similar to the untreated MCF 10A cells. Scale bars: 100  $\mu$ m. (C) Immunofluorescence analysis of p53-null Saos-2 cells treated with core fibrils using p53 and OC antibodies showing no endogenous p53 aggregation. Scale bar: 10  $\mu$ m. (D) Saos-2 cells showing no colony formation upon treatment with core fibrils even after 10 days of incubation similar to the untreated cells. Scale bars: 10  $\mu$ m. Images in A–D are representative of  $n=3$  independent experiments. (E) A soft agar colony formation assay was performed using untreated and treated MCF 10A and Saos-2 cells. Quantification of the number of colonies for all assays was done at Day 10. The number of colonies formed in the treated cells was comparable to the untreated control for both MCF 10A and Saos-2 cells. For MCF 10A cells, the  $P$ -values for comparison are as follows: untreated vs core monomer treated is 0.56553, untreated vs  $\alpha$ -synuclein fibril treated is 0.27908. For Saos-2 cells, the  $P$ -values for comparison are as follows: untreated vs core monomer treated is 0.80582, untreated vs core fibril treated is 0.6932 and untreated vs  $\alpha$ -synuclein fibril treated is 1.00000. ns, not significant. (F) qRT-PCR data showing the expression levels of genes linked with p53 pathways, namely p21 (*CDKN1A*), the pro-cancer gene *MAPK1* (MAPK) and the anti-cancer gene *BAX* are analyzed in MCF 10A and Saos-2 (p53-null cells) with various treatments. The fold change levels are firstly normalized to *GAPDH* expression levels and expression levels in untreated cells are further subtracted to obtain the normalized fold change levels. The bars represent mean  $\pm$  s.e.m.,  $n=4$  experimental datasets. The values show that gene expression levels do not alter significantly (low fold change values) after treatment with core monomer and  $\alpha$ -synuclein fibrils in the case of MCF 10A cells. In the case of Saos-2 p53-null cells, the *BAX* and *MAPK* levels are mostly unaltered (overall low fold change values) upon core monomer and  $\alpha$ -synuclein fibril treatment, which is similar to what is seen in the untreated cells. The values are plotted as mean  $\pm$  s.e.m.,  $n=4$  individual data sets. The statistical significance was calculated by one-way ANOVA followed by Bonferroni multiple comparison post-hoc test with a 95% confidence interval.

and repair during DNA replication (e.g. *TREX1* and *EXO1*) were downregulated (Fig. S5A). In contrast, anti-apoptotic genes and genes involved in chromatin remodeling (*AKT1*, *SEPT4*, *BAD*, *KDM4B* and *HDAC1*) were upregulated. Furthermore, the data showed upregulation of genes, *ERBB2* (Her2), *MAP2K1* and *EGF*, which are involved in promoting cell growth, signaling and proliferation (Fig. 3E; Fig. S5A). The data indicate that p53 amyloid formation at an early passage (T1) caused an immediate and drastic effect on tumor suppressive pathways of the cell (Fig. 3D,E; Fig. S5A). At the T5 stage, however, the regulatory genes associated with cell cycle and cell division (such as *CDCA2* and *CDC45*) showed decreased expression; whereas genes having a role in cellular architecture, migration and growth (such as *PECAM*, *WNT11* and *STAT3*) showed enhanced expression (Fig. 3F; Fig. S5B). Interestingly, *MDM2*, the major negative regulator of

p53 (Moll and Petrenko, 2003), also shows no increase in expression ( $\sim 0.8$ -fold change) in both T1 and T5 passages. As *MDM2* expression is regulated by the native transcriptional activity of p53 (Moll and Petrenko, 2003), *MDM2* expression might also be affected by p53 amyloid formation. Moreover, *KRAS* and multiple protein kinase signaling pathway genes involved in many cancers (Martin, 2003) were also upregulated in our datasets at both T1 and T5 passages (Fig. 3E,F; Fig. S5A,B). Hence, transcriptome analysis suggests that immediately after amyloid induction in cells (at the initial stage T1), p53 loss of function is more prevalent whereas, at a later stage, the gain-of-oncogenic function pathways are seen to be significantly altered, which is directly responsible for the tumorigenic nature of the T5 stage of cells. The gene expression pattern is also consistent with our phenotypic changes associated with core fibril-treated cells (Fig. 1).

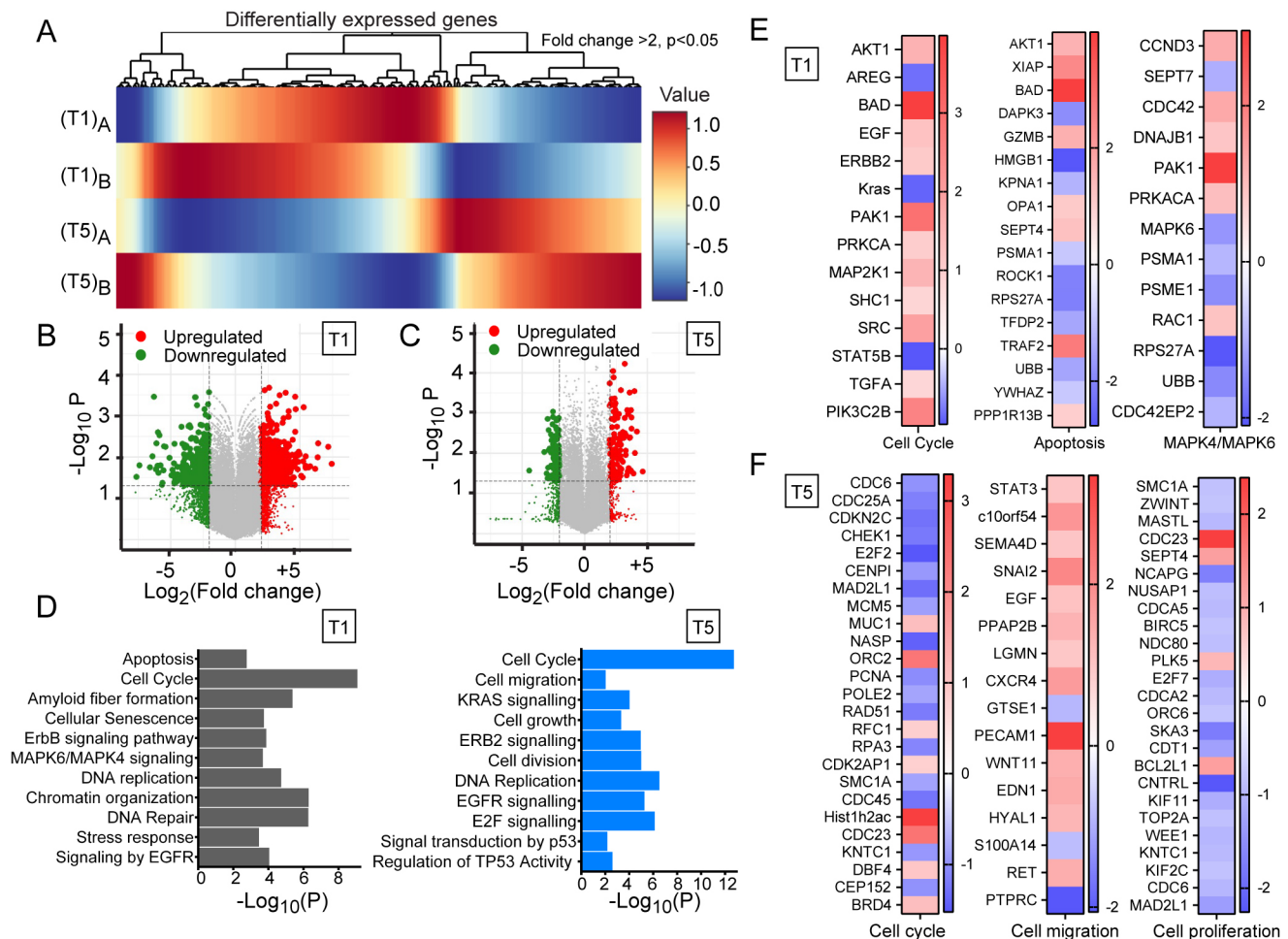


**Fig. 3. Gene expression analysis by microarray showing pathways affected by p53 amyloid formation.** (A) Heatmap of genes that are differentially regulated upon core fibril treatment in MCF 10A cells (for two different passages, T1 and T5). (T1)<sub>A</sub> and (T1)<sub>B</sub> are two biological replicates for the T1 passage. Similarly, two biological replicates were performed for cells at the T5 passage. (B,C) Volcano plots representing the  $\log_2$  fold change plotted against the  $-\log_{10} P$ -value at T1 and T5 passages, respectively. Differentially expressed genes are represented in large size dots of green (significantly downregulated) and red (significantly upregulated) color. The distribution showing a higher number of genes affected at the T1 passage as compared to the T5 passage. (D) Metascape analysis showing pathways that are significantly affected by p53 amyloid formation at T1 and T5 generations. At the T1 generation, cell cycle, apoptosis and DNA repair are significantly perturbed. The T5 generation shows perturbation of pathways involved in the cell cycle, DNA replication, cell migration and cell division. (E,F) Pathway analysis for gene expressions affected by p53 amyloid formation using the Metascape platform. Fold change of genes at T1 and T5 passages in the critically affected cellular processes were plotted with respect to the untreated control. Red color represents a relative increase in abundance, blue color represents a relative decrease, and white color represents no change. At T1, alterations in gene expression are associated with significant cellular processes such as cell cycle, apoptosis and MAPK signaling. At T5, alterations in gene expression are associated with processes such as the cell cycle, proliferation and migration.

Since epithelial-to-mesenchymal transition (EMT) is the process by which cancer cells lose their epithelial characteristics and acquire a mesenchymal phenotype (Brabletz et al., 2018), we further analyzed the expression levels of genes implicated in EMT (Fig. S5C) upon p53 amyloid formation in cells. EMT-associated genes were upregulated both at T1 and T5 passages as compared to the controls further indicating a gain of oncogenic phenotype by cells (Fig. S5C). For example, expression of mesenchymal gene markers [*FNI*, *CDH11*, *CDH2* and *VIM* (encoding vimentin)] and EMT-linked transcription factors/activators (*SNAI2* and *TGFB1*) was higher in cells with p53 amyloids at both T1 and T5. Cell surface proteins involved in cell-to-cell contact (*NOTCH2* and *VCAM1*) and intracellular signaling (*IL6* and *WNT5A*) showed increased expression values (Fig. S5D). Interestingly, many EMT genes showed much higher overexpression at T5 passage as compared to T1 passage such as *MMP1* (encoding matrix metalloproteinase 1) and *TGFB1* (encoding transforming growth factor  $\beta$ -1) (Fig. S5D).

Altogether, this indicates that genes regulating the EMT phenotype persist and progressively increase in expression from T1 to T5 passage, with the highest expression levels at T5 passage. This confirms that p53 amyloid formation and accumulation in cells can contribute to cancer progression and metastasis.

Next, to understand the alteration in the expression levels of direct targets of p53 due to amyloid formation, we mapped expression levels for a subset of genes ( $n=76$ ), which are a critical part of the p53 signaling network (Fig. 4A). The data showed that direct targets of p53 [such as p63 (*TP63*), p73 (*TP73*), *NOXA1*, *GADD45* (*GADD45A*) and *PCNA*] showed deregulation at both T1 and T5 generation (Fig. 4A). Since the amount of p53 amyloids gradually increase from passage T1 to passage T5, we evaluated the effect of accumulation of p53 amyloids on the expression of p53 target genes. We evaluated selective p53-linked genes for their relative expression from T1 to T5 passages using qRT-PCR across cell generations (Fig. 4B–D; Table S1). The direct p53 target p21

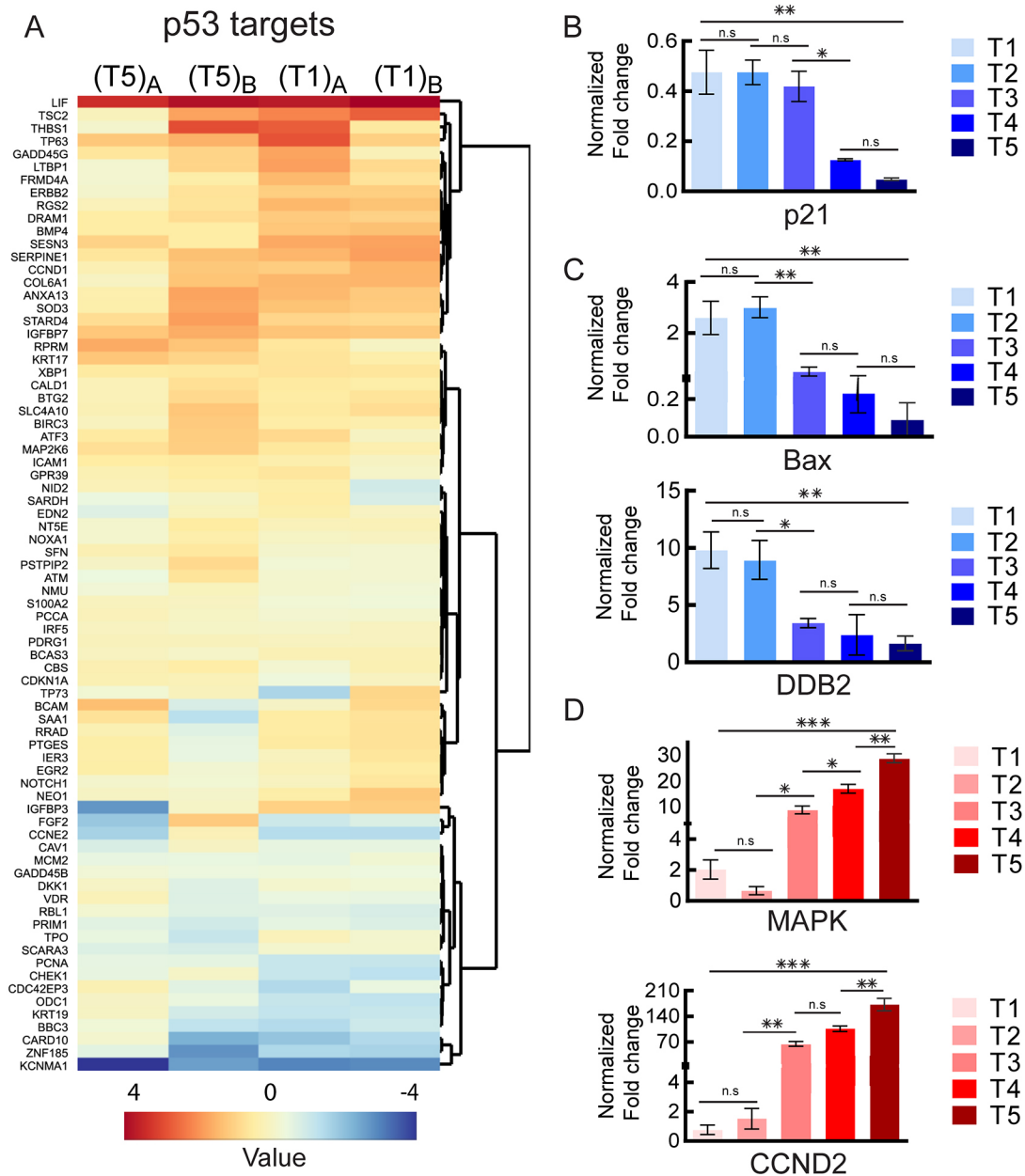


**Fig. 4. Alteration of gene expression of p53 targets due to amyloid formation of p53.** (A) Microarray data showing differential gene expression of p53 targets in terms of heat map for core fibrils treated cells as compared to untreated cells. Specific gene targets of p53, which are affected upon p53 amyloid formation are shown. Two biological replicates are shown for each passage: (T1)<sub>A</sub> and (T1)<sub>B</sub> for T1 generation and (T5)<sub>A</sub> and (T5)<sub>B</sub> are for T5 generation. (B–D) qRT-PCR data showing the extent of specific gene expression during various generations. The expression of genes linked with p53 pathways such as p21 (*CDKN1A*), pro-cancer genes [*MAPK1* (*MAPK*) and *CCND2*] and anti-cancer genes (*BAX* and *DDB2*) are analyzed. The expression of p21 decreased over the passages whereas pro-cancer genes were upregulated. The anti-cancer genes showed decreased expression over the passages. The values are normalized to the expression of GAPDH in the cells and represent mean  $\pm$  s.d.,  $n=2$  independent experiments (each set with three replicates). The  $P$ -values for all genes are as follows: p21 (T1 vs T2:  $>0.999$ , T2 vs T3:  $>0.999$ , T3 vs T4: 0.0254, T4 vs T5:  $>0.999$  and T1 vs T5: 0.0045); BAX (T1 vs T2:  $>0.999$ , T2 vs T3: 0.0091, T3 vs T4:  $>0.999$ , T4 vs T5:  $>0.999$  and T1 vs T5: 0.0092); DDB2 (T1 vs T2:  $>0.999$ , T2 vs T3: 0.048, T3 vs T4:  $>0.999$ , T4 vs T5:  $>0.999$  and T1 vs T5: 0.0092); MAPK (T1 vs T2:  $>0.999$ , T2 vs T3: 0.0162, T3 vs T4: 0.0161, T4 vs T5: 0.003 and T1 vs T5:  $<0.0001$ ); CCND2 (T1 vs T2:  $>0.999$ , T2 vs T3: 0.0084, T3 vs T4: 0.0533, T4 vs T5: 0.0068 and T1 vs T5:  $<0.0001$ ). \* $P<0.05$ ; \*\* $P<0.01$ ; \*\*\* $P<0.001$ ; ns, not significant. The statistical significance was calculated by one-way ANOVA followed by Bonferroni multiple comparison post hoc test with 95% confidence interval using Graphpad Prism.

(*CDKN1A*) showed decreased expression through the passages (Fig. 4B). Moreover, anti-cancer genes like *BAX* and *DDB2*, which are under direct transcriptional control of p53, showed downregulation (Fig. 4C). Concomitantly, pro-cancer genes like *CCND2* and *MAPK1* showed a gradual increase in expression across the passages (Fig. 4D). Altogether, this data suggests that p53 amyloid formation affects the pathways of the cell cycle, apoptosis

and pro-proliferative signaling, which leads to a gain of oncogenic phenotype in cells.

#### Comparison of gene expression due to p53 cancer-associated mutations versus p53 amyloid formation

p53 amyloids confer a malignant phenotype to the cells, which is similar to new oncogenic activities gained by several known

mutants of p53 (Oren and Rotter, 2010). It is known that mutant p53 proteins have variable phenotypic impacts on the central cellular pathways and differentially regulate gene expression in diverse cellular contexts (Weisz et al., 2007). We examined the differences in the transcriptional signatures due to wild-type p53 amyloid formation versus that driven by p53 mutations. We computed activity scores of the hallmark pathways from Molecular Signature Database (MSigDB) (Liberzon et al., 2015) in control MCF 10A cells, MCF10 A cells with p53 amyloids (microarray data from this study) and mutant p53 cancer cells lines (from data available in the literature; Adorno et al., 2009; Di Minin et al., 2014; Freed-Pastor et al., 2012; Girardini et al., 2011; Walerych et al., 2016). The mutant p53 dataset selected were R280K, R273H, R249S, M237I and R175H, which were experimentally overexpressed in breast cancer cell lines previously (Adorno et al., 2009; Di Minin et al., 2014; Freed-Pastor et al., 2012; Girardini et al., 2011; Walerych et al., 2016) (Fig. S6A). We found that out of 50 hallmark pathways, 13 pathways were dysregulated in amyloid-treated cells, which included prominent pathways such as EMT, hypoxia and other p53-regulated pathways (Fig. S6B). Similarly, 25 pathways were dysregulated in p53 mutated cells in total. Comparison of pathways significantly affected due to p53 amyloids and all p53 mutants ( $P < 0.01$ ) showed an overlap in nine pathways, including the p53 pathway and Kras signaling (Fig. S6B). The overlapped processes due to p53 amyloids as well as p53 mutants contribute similarly to gain-of-function traits, indicating that p53 amyloids act in a similar manner to aggressive oncogenic p53 mutants.

To further highlight the similarities and differences in p53 mutants in comparison to p53 amyloids, we selected datasets of structural (with a role in the maintenance of native p53 structure; Joerger and Fersht, 2007) and contact mutants of p53 (role in direct DNA contact; Joerger and Fersht, 2007). The p53 structural mutants (R175H, R249S and M237I) showed an overlap of 12 pathways with p53 amyloid, including the p53 pathway, glycolysis and E2F targets (Fig. S6C). p53 contact mutants (R280K and R273H) also showed a similar effect on cellular pathways as the p53 amyloid dataset, with complete overlap between significantly altered hallmark pathways in both sets (Fig. S6D). Individual datasets of p53 structural mutant (R175H) and contact mutant (R273H) also showed a similar overlap with the p53 amyloid dataset (Fig. S6E). Taken together, the comparative analysis of these datasets suggests that p53 amyloid formation affects similar sets of cellular pathways to those linked to p53 cancer mutations. Hence, based on the overlap of pathways in each case, the amyloid formation of p53 impacts cellular pathways more compared to individual mutants, whereas it is equivalent in effect to all mutants combined. It is important to note that even though the gain of oncogenic function pathways adopted by p53 mutants and p53 amyloid show similarities, we speculate that unique individual gene level differences might also exist. This data, therefore, suggests that, similar to mutant p53, the alteration in the cellular paradigm due to p53 amyloid formation can also lead to gain-of-tumorigenic activities during tumorigenesis *in vivo*.

### Proteome-wide changes in cells due to p53 amyloid formation

Many of the protein level alterations linked with cancer are known to affect the signaling pathways that regulate cell growth, division, death and motility at the protein level (Giancotti, 2014). For understanding these signaling pathways, we further examined the proteome of p53 amyloid-containing cells to elucidate changes in

protein-protein interaction networks by using iTRAQ labeling coupled with liquid chromatography-tandem mass spectrometry (LC-MS/MS) analysis (Datta et al., 2017; Zhao et al., 2016). Similar to the microarray analysis, we profiled the p53 amyloid-containing MCF 10A cells at two different stages, initial (T1) and later (T5) generations. Expression levels of a total of 412 proteins at T1 and 261 proteins at T5 were found to be significantly altered due to core fibril treatment compared to the untreated control (Fig. 5A). We further mapped the altered proteins at T1 and T5 to their functional classes in terms of cellular localization and molecular function (Fig. S7A,B) using STRING (version 11.0) (Szklarczyk et al., 2019).

The data suggest that at T1 passage, proteins involved in the regulation of cell cycle (such as CDK1 and CCAR1), apoptosis (such as Bcl2 and PDCD6) and p53-dependent DNA damage checkpoints decreased significantly; whereas proteins involved in MAPK4 signaling (MAP3K10) and Wnt signaling showed higher expression levels (Fig. 5B,C). In the later generation (T5), however, the cell cycle regulatory proteins like CDC42 and proteins associated with cell death showed decreased levels (Fig. 6A). In contrast, the proteins implicated in translational machinery (such as EIF4 and EFF2) and cell proliferation pathways (such as CDK2, CRNKL1 and MAPK1) showed higher levels of expression (Figs 5B and 6A). Interestingly, at both T1 and T5, proteins in pathways governing ubiquitylation, UPR and proteasomal degradation machinery [UBP1, PRS10 (also known as PSMC6) and PSA3] were upregulated (Figs 5C and 6A).

Apart from these processes, chaperones belonging to Hsp70 and Hsp90 families showed significantly increased levels (Fig. 5C) at T1. The upregulation of proteasomal and chaperone machinery suggests activation of the cellular defense against the misfolded protein aggregates. In addition to this, we also found that at both T1 and T5 passages, proteins involved in metabolic processes, such as glycolysis, citric acid cycle and amino acid synthesis, showed increased levels of expression (Figs 5C and 6A). Cancer cells are known to alter metabolic pathways and display higher metabolic rates, which provide the cancer cells with a growth advantage over normal cells (Hsu and Sabatini, 2008). These upregulated metabolic proteins suggest that carbohydrate and protein metabolism in p53 amyloid cells is significantly altered, contributing to the proliferation and/or survival.

From the array of proteins, we further analyzed the p53-centric cluster of differentially expressed proteins to establish the changes in p53 mediated regulation (Fig. 6B,C). At T1, we observed that p53 amyloid formation led to perturbation of cell cycle regulation by affecting the expression levels of key proteins involved in cell cycle checkpoints (Fig. 6B). For instance, the amyloid formation of p53 prevents its critical function of maintaining the levels of cyclin-dependent kinases and cyclin-dependent kinase inhibitors, such as CDK1 and CDKN1A (p21), respectively (Fig. 6B). Furthermore, upregulation of cell division cycle proteins (CDCs) is observed. Parallely, the proteins in signaling pathways of the cell required for proliferation like MAPK proteins, EGFR, AKT proteins, and phosphatidylinositol 3-kinases (PI3Ks) are upregulated (Fig. 6B). In contrast, p53 transcription-mediated apoptotic control might get significantly impacted as evidenced by the lowered expression of pro-apoptotic proteins like BAX, BAD and CASP3. Furthermore, at the T5 passage, the proteins associated with proliferative pathways continue to be overexpressed (Fig. 6C), consistent with the gene expression profile. The apoptotic signaling is severely compromised, although pro-apoptotic proteins are not significantly detected at the later passage (Fig. 6C), suggesting oncogenic addiction of the cells to proliferative signaling

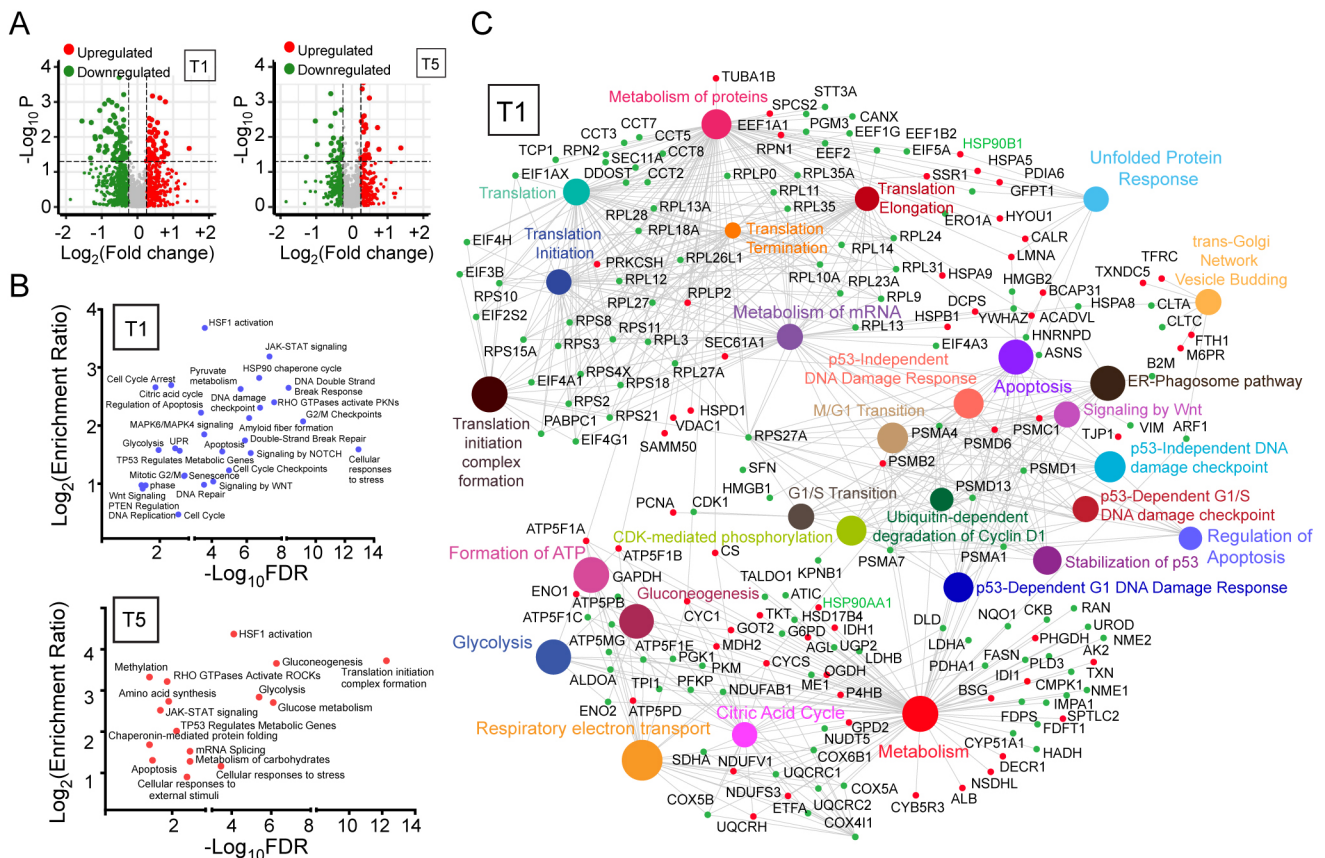


**Fig. 5. Changes in proteome due to p53 amyloid formation in cells.** (A) Volcano plot displaying  $\log_{10}(P\text{-value})$  vs  $\log_2$  fold-change values corresponding to differentially expressed proteins in cells containing p53 amyloid at T1 passage (left panel) and T5 passage (right panel). The red dots represent the overexpressed proteins and the green dots represent the proteins with lowered expression compared to the untreated control cells. More proteins are affected at the T1 passage than at the T5 passage. (B) False discovery rate (FDR) and enrichment ratio of differentially expressed proteins with significantly altered signaling pathways were calculated from the Reactome database.  $\log_2(\text{enrichment ratio})$  was plotted against the  $-\log_{10}(\text{FDR})$  for both T1 and T5 passages. Proteins enriched at the T1 passage indicating that apoptosis, cell cycle, senescence and DNA damage repair pathways are significantly affected. The pathways linked to glucose metabolism are substantially upregulated, possibly contributing to the higher survival of the cells (upper panel). At T5, cells harboring p53 aggregates showing significant changes in apoptotic pathways and several signaling pathways (such as JAK-STAT and Ras). (C) Network analysis of proteins that are significantly altered upon fibril treatment to the cells (at T1) was performed using NetworkAnalyst 3.0. A bubble plot representing proteins as nodes and the clusters of proteins as dense circles in particular pathways is shown. At T1, proteins that belong to the pathways regulating apoptosis, cell cycle and senescence of cells were altered and proteins involved in carbohydrate metabolism also showed a higher level of expression. Data shown are from  $n=3$  independent experiments.

(Weinstein and Joe, 2008). Overall, unregulated cell cycle progression and high expression levels of pro-proliferative proteins induce transformative traits in the cells.

### Inhibition of pathways involved in p53 amyloid-mediated transformation

We further examined the dependency of cells with p53 amyloids on the proliferative signaling pathways to maintain the transformative traits. To do this, we considered the pathways that are affected both at T1 and T5 passages (Fig. 7A). The pathways linked to cell cycle progression, proliferation and MAPK signaling were common in T1 and T5 passages (Fig. 7A).

When we evaluated the significantly affected genes or proteins in these pathways, we found that the cell cycle and MAPK signaling pathways are highly altered at both transcriptomic and proteomic levels in cells with p53 amyloids (Fig. 7B). From this analysis, it is also evident that CDK proteins from the cell cycle pathway and MAPK proteins are highly altered in transformed cells with p53 aggregates in comparison to normal cells (Fig. 7A,B). Therefore, we targeted the CDK and MAPK proteins using well-established chemical inhibitors – flavopiridol hydrochloride hydrate (FP)

(Carlson et al., 1996) and PD98059 (Alessi et al., 1995), respectively. The apoptotic population of cells in the presence of various concentrations of FP was analyzed in comparison to the untreated control (Fig. 7C, left panel). Treatment with FP led to a rapid increase in apoptotic population in the cells with p53 amyloids as compared to the control untreated cells at both T1 and T5 passage. Similarly, core-transformed cells after treatment with the MAPK inhibitor PD98059 showed a drastic loss of cell viability as compared to the untreated cells (Fig. 7D, left panel). The data showed that the  $EC_{50}$  for treatment with FP and PD98059 was significantly lower for the core-transformed cells as compared to the untreated MCF 10A cells (Fig. 7C,D, right panels). MCF-7, a breast cancer cell line used as a cancer cell control, were also treated with FP and PD98059. The viability of MCF-7 cells also decreased with the increasing concentration of these compounds (Fig. S8A). It is important to note that, as previously reported (Zhao et al., 2017), a higher concentration range was needed to achieve the loss of viability for aggressively transformed MCF-7 cells. The survival curve and the comparison of  $EC_{50}$  values of the T1 and T5 passages show that the cells at the T5 passage had a lowered survival trend as compared to the T1 passage for both treatments (Fig. 7C,D;



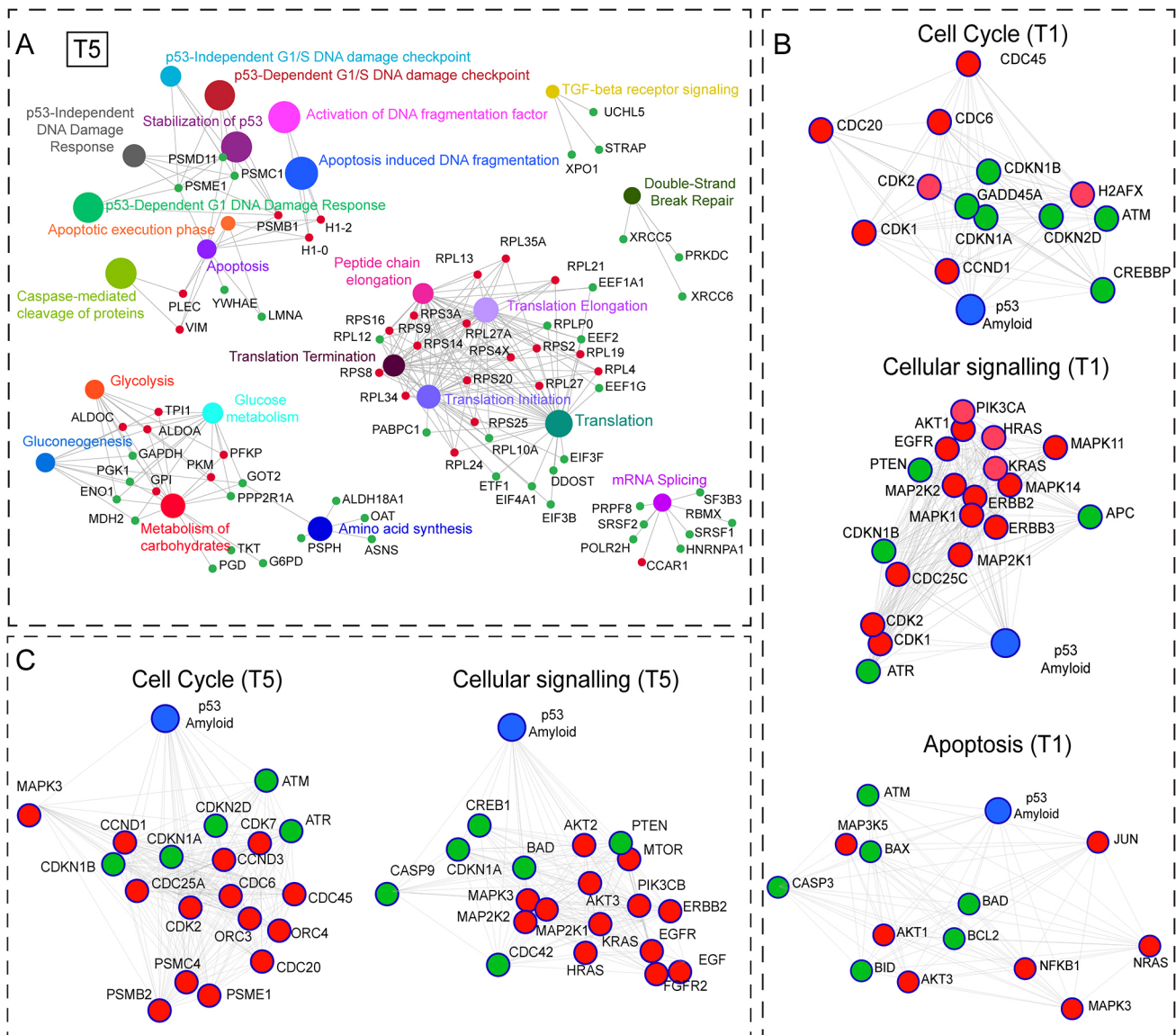


**Fig. 6. Significantly affected protein–protein interactions at T5 passage and p53-specific changes in cell signaling.** (A) Network analysis (using NetworkAnalyst 3.0) of cells harboring p53 amyloids at the T5 stage showing changes in proteomic profiling associated with various pathways including apoptotic and signaling pathways (such as JAK-STAT and Ras). In the network, proteins are represented as nodes and clusters of proteins are represented as dense circles. Apart from apoptosis and DNA damage checkpoints, the proteins associated with metabolic pathways and translational machinery also show increased expression, reminiscent of cancer cells. (B,C) Network analysis of differentially regulated p53 target proteins altered upon p53 amyloid formation using the NetworkAnalyst 3.0 platform. The red bubbles represent the upregulated p53 target proteins; whereas the green bubbles represent downregulated proteins. In both T1 and T5 passages, cell cycle progression is dysregulated due to the loss of inhibitory proteins like CDKN1 and the enhanced expression of cyclin-dependent kinases like CDK1. The proteins involved in regulatory control of tumor suppressive pathways like apoptosis showing downregulation at the initial passage T1. In contrast, the proliferative pathways involving MAPKs (MAPK1, MAP2K1 and MAP2K2), phosphatidylinositol kinases (PIK3CA) and Ras signaling (Hras, Kras) showed upregulation in the cells with p53 amyloids at T1. However, the cells at later passage (T5) showing an increased oncogenic dependency on the proliferative pathways. Data shown are from  $n=3$  independent experiments.

Fig. S8B). This suggests that cells with p53 amyloids at the T5 passage might be affected more upon inhibitor treatment than those at T1. This indicates that cells at the T5 passage might be highly dependent on CDK and MAPK proteins for maintaining their oncogenic phenotype as compared to the T1 stage.

To further validate this, we specifically targeted CDK1, which was observed to be overexpressed in cells with p53 amyloids (Fig. 7B,C), by siRNA-mediated knockdown at T1 and T5 stages. Western blotting analysis showed >90% knockdown of CDK1 expression at a siRNA transfection concentration of 30 nM (Fig. 7E; Fig. S8C), which was used for further assays. The non-specific

siRNA was used as a negative control, which did not affect the CDK1 levels (Fig. 7E; Fig. S8C). We evaluated the cell viability after CDK1 knockdown in core-treated and untreated cells in the presence of actinomycin D (ActD) as an apoptotic stressor (Kleeff et al., 2000). Analysis of an Annexin V–FITC/propidium iodide (PI) apoptosis assay using fluorescence-activated cell sorting (FACS) showed that the knockdown of CDK1 effectively led to a reduction in viability by >20% (with only CDK1-specific siRNA), whereas in the presence of ActD the viability was reduced by >50% (with CDK1-specific siRNA and ActD) (Fig. 7F). Overall, these data suggest that the loss of CDK1 expression is detrimental to the core

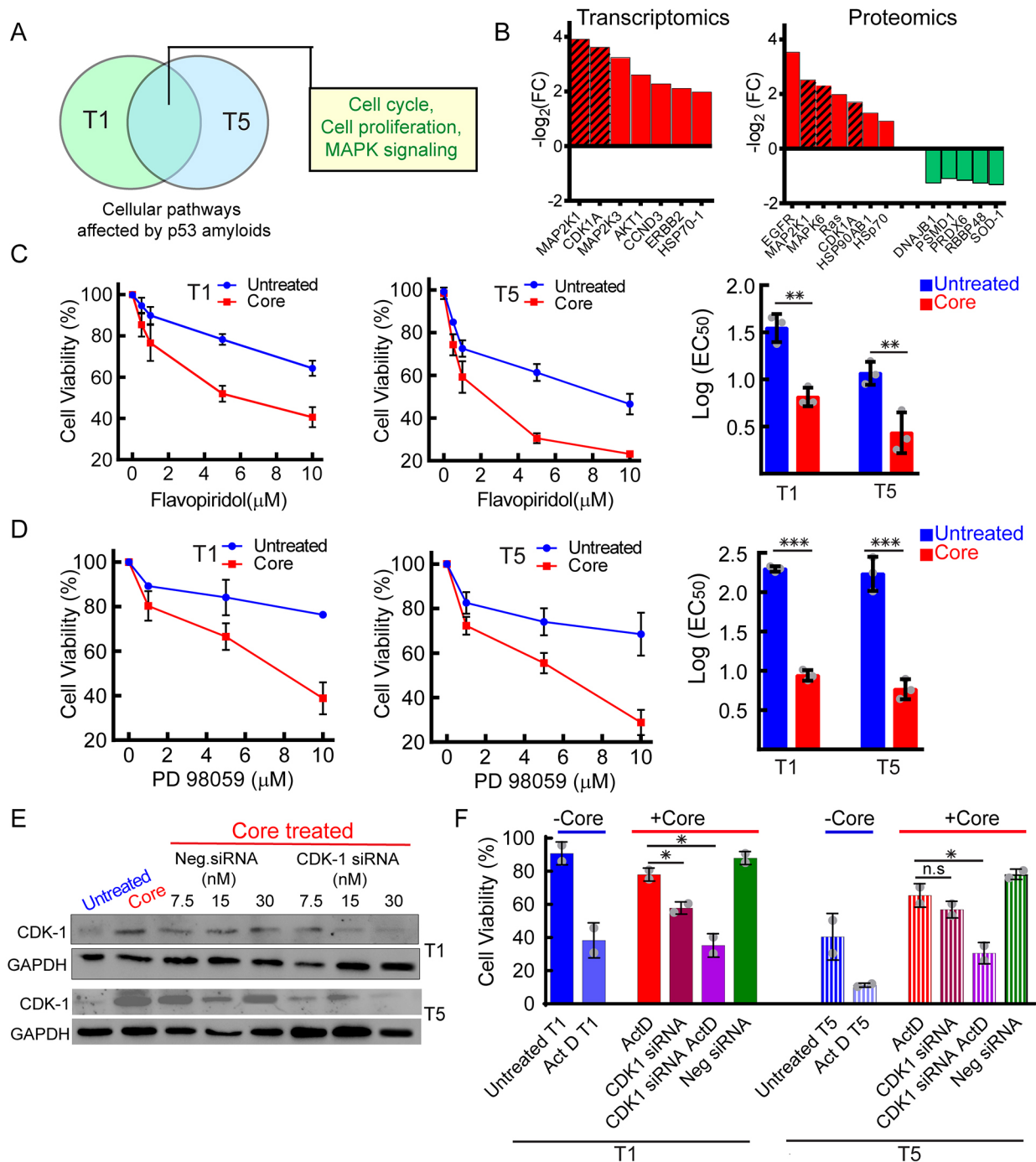


Fig. 7. See next page for legend.

amyloid transformed cells indicating a role of CDK1 in maintaining the proliferative and tumorigenic traits of these cells.

**DISCUSSION**

Aggregation and amyloid formation of proteins most often results in the loss of their functions and gain of toxic functions, which could be the potential cause of cell death occurring in various neurological disorders, such as Alzheimer’s and Parkinson’s diseases (Koo et al., 1999). However, past studies have suggested that amyloid formation can also be involved in a functional state (functional amyloids), evolved for the native function in the host organism (Fowler et al., 2007). For example, yeast prion provides survival benefits to the

yeast against environmental stress (Alberti et al., 2010; Halfmann et al., 2012; Serio and Lindquist, 2001). Similar to this situation, it has been shown that p53 misfolding and aggregation not only result in loss of p53 tumor suppressor functions but also might end up with oncogenic gain-of-function (Lasagna-Reeves et al., 2013; Navalkar et al., 2020; Xu et al., 2011). This is similar to what is seen with most of the cancer-associated p53 mutations (Oren and Rotter, 2010; Stein et al., 2019), which are known to act as oncogenes. We have previously demonstrated that amyloid formation of full-length endogenous p53 amyloid in cells upon the addition of p53 core fibril seeds (a handle for inducing full-length p53 amyloid formation) leads to accumulation of oncogenic traits in cells (Navalkar et al.,

**Fig. 7. Inhibition of pathways involved in p53 amyloid mediated transformation.** (A,B) Selection of target pathways linked to p53-amyloid mediated transformation. Microarray and proteomics analysis showing that p53 amyloid formation predominantly affects the cell cycle and proliferative pathways. CDK and MAPK pathway proteins are substantially affected both at T1 and T5 passages. Bars marked with hatchings indicate genes and proteins linked with CDK and MAPK pathways. Data compared from  $n=2$  independent experiments. (C) Treatment of p53 core amyloid-transformed cells with increasing concentrations of the CDK inhibitor flavopiridol (FP) at T1 (left panel) and T5 passages (middle panel) showing a decrease in cell survival. The right panel shows the corresponding  $EC_{50}$  values. The untreated cells were used as a control. The amyloid-transformed cells showed increased apoptosis upon FP treatment as measured by an MTT assay. The  $P$ -value for T1 passage (untreated vs core treated) is 0.00208 and for T5 passage (untreated vs core treated) is 0.01175. (D) Treatment of p53 core amyloid-transformed cells at T1 (left panel) and T5 passages (middle panel) with increasing concentrations of the MAPK inhibitor PD 98059. The right panel shows the corresponding  $EC_{50}$  values. The amyloid-transformed cells showed significantly higher apoptosis upon PD 98059 treatment as measured by MTT assay. The untreated cells were used as a control and did not show significant toxicity in both cases. T5 passage showed a significantly higher effect of FP and PD98059 treatment. The  $P$ -value for T1 passage (untreated vs core treated) is  $<0.0001$  and for T5 passage (untreated vs core treated) is 0.00054. Results in C,D are given as mean $\pm$ s.e.m ( $n=3$ ). (E) siRNA-mediated knockdown of CDK1 in cells with p53 amyloids at T1 and T5 passage. 30 nM siRNA showing the maximum knockdown of CDK1 with around  $>90\%$  reduction in the levels of CDK1. Image representative of  $n=2$  experiments. (F) Annexin V–FITC/PI apoptosis assay showing that the knockdown of CDK1 increased the susceptibility of core-transformed cells to stressor-induced apoptosis. The cell viability was reduced by  $>20\%$  with CDK1-specific siRNA and further by  $>50\%$  with the addition of ActD for both the passages. The non-specific siRNA transfection (negative control) did not show any loss of viability. The  $P$ -values are as follows: at T1 (ActD vs CDK-siRNA: 0.0339 and ActD vs CDK-siRNA with Act D: 0.01742) and at T5 (ActD vs CDK-siRNA: 0.29749 and ActD vs CDK-siRNA with Act D: 0.03565). Results are given as mean $\pm$ s.d ( $n=2$ ). \* $P<0.05$ ; \*\* $P<0.01$ ; \*\*\* $P<0.001$ ; ns, not significant. The statistical significance was calculated by one-way ANOVA followed by Bonferroni multiple comparison post hoc test with a 95% confidence interval.

2021). Furthermore, we showed that p53 amyloids possess prion-like inheritable properties, such as the transfer of advantageous traits from one generation to another generation (Navalkar et al., 2021). We asked whether, immediately upon amyloid induction in cells and due to gradual cell to cell transmission, p53 amyloids can provide survival advantages to cells leading to the alterations of various cellular pathways and acquisition of tumorigenic properties.

We analyzed cells with p53 amyloids at initial and later passages to decipher the gradual effect of p53 amyloid formation on cellular pathways (Fig. 1). Our data show that cells at later passage acquire aggressive cancer-like properties, such as enhanced survival, resistance to senescence/aging and increased colony-forming propensity compared to cells which encounter immediate amyloid formation at early passages. The microarray and proteomics data show that p53 amyloid formation can lead to the downregulation of the tumor-suppressive and regulatory pathways at an early stage of aggregation and gradually introduce gain of oncogenic function via the upregulation of the cell cycle and cell proliferation pathways (Figs 3–6). Inhibition of amyloid-specific transformative proteins associated with the CDK and MAPK pathways reduced cell survival, further indicating that cells at initial and later passages are heavily dependent on CDK and MAPK proteins for maintaining their oncogenic phenotype (Fig. 7). The effect of inhibitory compounds against these key molecules was higher at later passages suggesting that cells at later passages have increased oncogenic addiction to these pathways.

Furthermore, the upregulation of UPR and the chaperone machinery (Hsp70 and Hsp90 proteins, which are involved in the

folding of p53; Boysen et al., 2019) in response to p53 amyloids in the cells (Figs 5 and 6) was also observed. Such changes in protein homeostasis were also demonstrated when cells were treated with artificial  $\beta$ -sheet proteins that were designed to form amyloid-like fibrils (Olzschka et al., 2011). This indicates that apart from p53-specific pathways, p53 amyloid formation also causes aberrant changes in protein quality control and clearance mechanisms (Fig. 5). In addition, the partial degradation of p53 amyloids could create secondary infectious protein aggregates (seeds), aiding in cell-to-cell transmission along with the inheritable prion-like p53 transmission (Brachmann et al., 2005; Halfmann et al., 2012; Liebman and Chernoff, 2012; Masison and Wickner, 1995; Wickner et al., 2004, 2015, 2000). In this context, strategies that target p53 misfolding and aggregation have been implemented in the recent decade (Palanikumar et al., 2021; Rangel et al., 2019; Soragni et al., 2016), highlighting the clinical relevance of these observations.

### Mechanism of p53 amyloid-mediated cellular transformation

Based on the evidence from the microarray and proteomic screens, we propose the cellular pathways as depicted in Fig. 8. p53 in its native form acts as a transcription factor, which upon misfolding and amyloid formation in the cytoplasm and/or in the nucleus, cannot bind to its cognitive response element for its transcriptive function (Ghosh et al., 2017; Navalkar et al., 2021). Therefore, cells with p53 amyloids show a loss of p53 native function in terms of apoptotic and cell cycle arrest pathways at the initial stage (Figs 3 and 4). Additionally, the p53 amyloids also confer an unlimited growth advantage to cells by upregulating signaling pathways involved in cell cycle progression and proliferation. A concomitant gain of oncogenic functions via increased proliferative signaling and a higher rate of metabolism rewires the cellular pathways, leading to a cancer-like phenotype (Fig. 8). Our data indicate that the increased rate of translation and metabolism in these cells also supports their increased survival rate over cell generations and lowers the senescence rate as compared to cells without p53 amyloids (Fig. 1). This selective oncogenic addiction of cells with p53 amyloids can also lead to transformation into metastatic cancer cells. Apart from p53-associated changes, these cells also show elevated levels of chaperone proteins at the earlier passages as a part of the UPR. These changes in chaperone levels are also seen to be associated with other amyloid-linked diseases like Parkinson's and Alzheimer's disease (Hartl et al., 2011; Kriegenburg et al., 2012).

In conclusion, our work points out several downstream effects of p53 amyloids, which might explain the widespread observation of p53 amyloid in cancers and how p53 amyloids can act as an oncogenic factor (Fig. 8). Our work can be used to develop strategies that enhance tumor suppressive proteins or inhibit the expression of addictive oncogenic pathways. Such approaches will be powerful tools with therapeutic potential against a subset of cancers with p53 amyloids.

## MATERIALS AND METHODS

### Chemicals and reagents

All chemicals used were of the purest quality and were purchased from Merck Millipore (Darmstadt, Germany) or Sigma-Aldrich (St Louis, MO, USA). Double-distilled and de-ionized water was used from Milli-Q system (Millipore Corp., Bedford, MA, USA) and autoclaved before use.

### p53 core domain expression and purification

p53 core protein was expressed and purified according to our published protocol (Ghosh et al., 2017) with p53 core domain plasmid (Addgene #24866). Briefly, the p53 core domain plasmid was transformed in *E. coli* BL21 (DE3) to express p53 core protein with His6 tag at N-terminus. 1 mM isopropyl  $\beta$ -D-1-thiogalactopyranoside (IPTG, Himedia, India) was used to

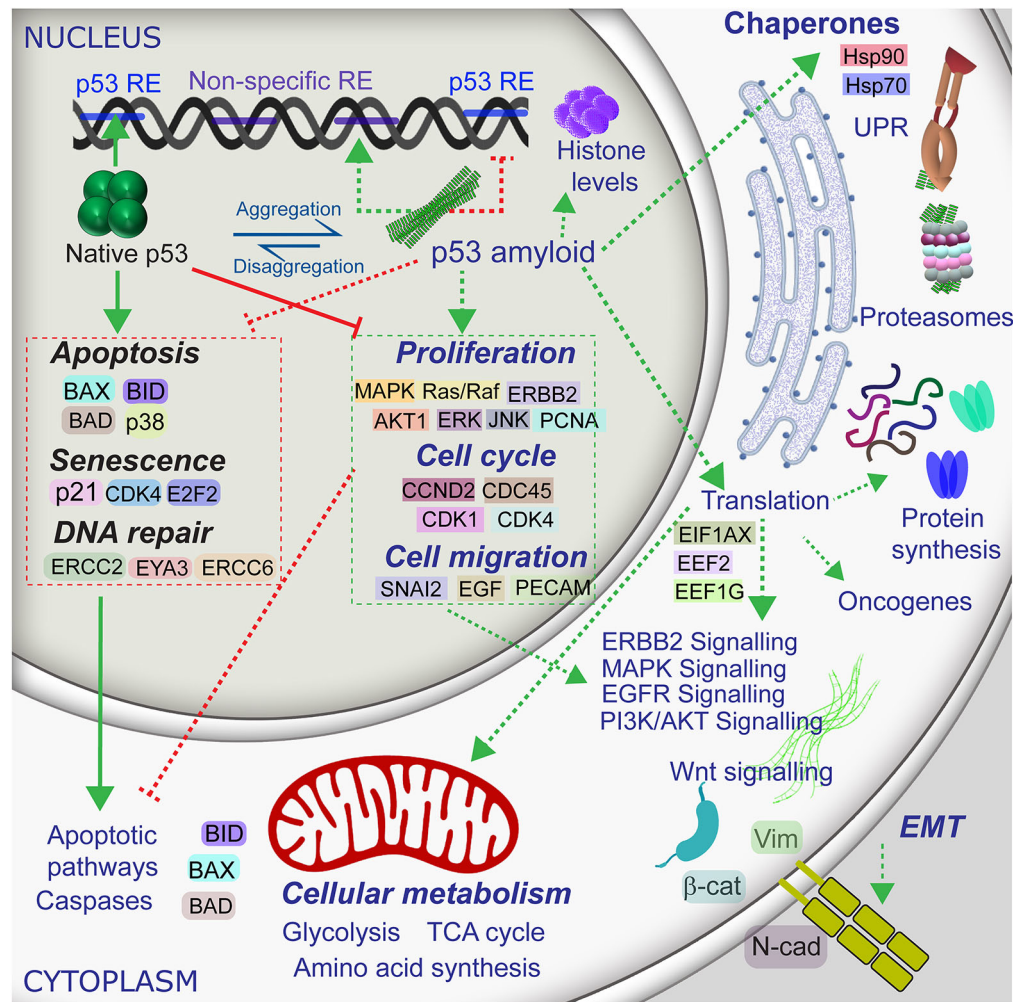


**Fig. 8. Model of pathways affected by p53 amyloid formation in cells.** A mechanistic model of the cellular consequences due to p53 amyloid formation based on the microarray and proteomic analysis of cells harboring p53 aggregates. Solid and dotted arrows indicate processes affected by native p53 and amyloid form of p53, respectively. The red and green color of arrows indicate negative regulation and positive regulation, respectively. p53 is a tumor suppressor protein, which regulates the expression of a plethora of downstream genes protecting the cells from the cancerous phenotype. Native p53 functions as a transcription factor in tetrameric form and binds to p53-specific response element (RE) to regulate the apoptotic, senescent and DNA repair pathways via multiple players. Native p53 also governs cell cycle and proliferation to maintain cellular homeostasis. Amyloid formation of p53 reverses its tumor-suppressive role and confers the gain of oncogenic function to the cells by modulation of cellular networks involved majorly in the cell cycle, DNA repair and cell proliferation. Pathways implicated in UPR, chaperones (Hsp70 and Hsp90 proteins) and proteasomal machinery are highly upregulated due to amyloid formation. Owing to p53 amyloid formation, genes and proteins involved in apoptotic and senescence pathways (such as BAX and BID) are downregulated making the cell vulnerable to oncogenic transformation. Concurrently, as a downstream consequence, genes involved in cellular signaling, which induce proliferation and cell cycle (CDKs, MAPKs, ERKs, CDCs and Ras) are upregulated due to p53 amyloid formation. These pro-oncogenic genes confer growth, migratory and survival advantages to cells harboring p53 aggregates. Furthermore, the upregulation of proteins in translational and metabolic pathways supports the prolonged survival of these cells. p53 amyloid formation, thus, might affect the multistep process of malignant transformation, contributing differentially to cancer initiation, progression and metastasis.

induce expression at 25°C, overnight. The cell pellet was lysed in 50 mM sodium phosphate pH 8.0 containing 300 mM NaCl and 1 mM PMSF (Sigma-Aldrich). The cell pellet was sonicated at 40% amplitude for 15 min (3 s ON; 3 s OFF pulse). The cell lysate was centrifuged and supernatant added to Ni<sup>2+</sup>-sepharose affinity chromatography column to purify His-tagged p53 core protein using an imidazole gradient. The protein was dialyzed using 50 mM sodium phosphate buffer with 300 mM NaCl, pH 7.4. Protein elution was confirmed using 12% SDS-PAGE gels, and the concentration was estimated by UV absorption. The molar absorptivity of protein ( $\epsilon$ ) is 17,420 M<sup>-1</sup> cm<sup>-1</sup>

#### Aggregation of p53 core domain *in vitro*

p53 core monomer protein at a concentration of ~50  $\mu$ M (500  $\mu$ l) in 50 mM sodium phosphate buffer (pH 7.4, containing 0.3 M NaCl, 0.01% sodium azide) and equimolar concentration of chondroitin sulphate A (CSA, Sigma-Aldrich, USA) dissolved in the same buffer were mixed. Protein was used for setting up *in vitro* aggregation according to the

previously published protocol (Ghosh et al., 2017). For this, the p53 core protein was incubated at 37°C for 96 h with slight agitation in the presence of chondroitin sulphate A. The fibrillar aggregates were centrifuged at 200,000 *g* for 45 min at 4°C and resuspended in PBS, pH 7.4. Fibril formation was confirmed using ThT fluorescence, CD spectroscopy and electron microscopy as described previously (Navalkar et al., 2021).

#### Preparation of FITC-labeled p53 core fibrils

p53 core fibrils were pelleted by ultracentrifugation (200,000 *g*) for 45 min at 4°C using a Beckman Coulter Optima Max-XP ultracentrifuge with TLA-100 fixed-angle rotor. The pelleted fibrils were used for labeling with a fluorescent probe (FITC) as per the manufacturer's recommendation (Thermo Fisher Scientific, USA). For this, the pelleted fibrils were resuspended in 0.1 M sodium bicarbonate buffer, pH 9. FITC solution (4-molar excess, dissolved in DMSO) was slowly added to the fibril solution and incubated for 4 h with constant stirring (150 rpm) at 4°C. After 4 h, the

reaction mixture containing fibrils was collected by ultracentrifugation at 200,000 *g* for 45 min at 4°C. The unreacted dye was removed by frequent washes and ultracentrifugation at 200,000 *g* for 45 min at 4°C. Finally, the labeled core fibril pellets were dissolved in sterile PBS.

### Cell culture

The non-tumorigenic human breast epithelial MCF 10A, MCF-7 and Saos-2 (human osteosarcoma) cells used in the study were obtained from the National Centre for Cell Science, Pune, India. For culturing MCF 10A cells, Dulbecco's modified Eagle's medium (DMEM, Gibco, USA) with horse serum (5% Gibco, USA), hydrocortisone (0.5 µg/ml, Himedia, India), hEGF (20 ng/ml, Invitrogen, USA), insulin (10 µg/ml, Himedia, India) and antimicrobial agent penicillin-streptomycin (1×, Himedia, India) was used. Cells were passaged when 80% confluency was achieved. Assay medium was used for all experiments with MCF 10A. The assay medium is DMEM growth medium (Gibco, USA) supplemented with horse serum (2%, Gibco, USA), hydrocortisone (0.5 µg/ml, Himedia, India), insulin (10 µg/ml, Himedia, India) and penicillin-streptomycin (1×, Himedia, India). Saos-2 cells were maintained in McCoy's 5A medium (Sigma Life Science; #M4892-1L, Modified, L-Glutamine) supplemented with 15% FBS (Gibco, USA; #10270-100), sodium bicarbonate (3.7 g/l) and 1× penicillin-streptomycin (Himedia, India) antimicrobial agent. MCF-7 cells were maintained in DMEM medium (Gibco, USA) supplemented with 10% FBS (Gibco, USA; #10270-100), sodium bicarbonate (3.7 g/l) and 1× penicillin-streptomycin (Himedia, India) antimicrobial agent. All cell lines were maintained at 37°C with 5% CO<sub>2</sub> and 95% humidity.

### Fibril treatments and passaging of cells

We prepared the p53 core fibrils seeds as per the previous protocol (Navalkar et al., 2021) using sonication. For the aggregation of endogenous p53, 30 µM of core fibril seeds were added to 1 ml DMEM growth medium (Gibco, USA) supplemented with horse serum (2%, Gibco, USA), insulin (10 µg/ml, Himedia, India), hydrocortisone (0.5 µg/ml, Himedia, India) and penicillin-streptomycin (1×, Himedia, India). Cells were passaged when 80% confluency was achieved. For passaging to get the next generation, ~1% of cells from the previous generation were mixed with assay medium and added to a fresh well. Untreated cells were passaged similarly.

### α-Synuclein purification and labeling

Expression of recombinant α-synuclein was performed in *E. coli* BL21 (DE3) cells using pRK172 plasmid construct and purified as per established protocols (Volles and Lansbury, 2007) with slight modifications (Singh et al., 2013). The purity of the protein was validated by SDS-PAGE followed by MALDI-TOF mass spectrometry. Low molecular weight (LMW) α-synuclein was used for labeling and subsequent fibrillation studies. We prepared LMW α-synuclein as per the previously established protocols (Ghosh et al., 2013; Singh et al., 2013). Briefly, lyophilized protein was dissolved in 20 mM Gly-NaOH buffer (pH 7.4) containing 0.01% sodium azide, and dialyzed (using 10 kDa membrane) against the same buffer. The protein solution was then passed through 100 kDa MW cut-off filters (Centricon YM-100, Millipore) and the flow through containing monomeric protein was collected and used for labeling and aggregation studies. The monomeric α-synuclein was labeled with fluorescent probe (NHS-Rhodamine) as per manufacturer's recommendations (Thermo Fisher Scientific, Molecular Probes, USA). For preparing labeled α-synuclein fibrils, unlabeled monomeric protein (90%) was mixed with Rhodamine-labeled protein (10%) at a protein concentration of 300 µM in 20 mM Gly-NaOH buffer, pH 7.4 (containing 0.01% sodium azide). The microcentrifuge tube containing the protein solution was incubated at 37°C in a rotational shaker (EchoTherm model RT11; Torrey Pines Scientific, USA) with slight agitation. The β-sheet conformation of labeled fibrils and fibrillar morphology was confirmed by CD spectroscopy and transmission electron microscopy (TEM) analysis.

### Internalization of α-synuclein amyloid seeds

MCF 10A or Saos-2 cells (1×10<sup>4</sup> cells per well) were seeded on 12 mm coverslips in a 24-well plate (Corning, USA). Cells were then treated with

250 nM of Rhodamine-labeled α-synuclein fibril seeds and incubated for another 48 h at 37°C. α-Synuclein amyloid seeds were prepared by controlled sonication (Sonics & Amp, Materials Inc., USA) with pulse (3 s ON; 1 s OFF) amplitude (20%) for 3 min, and used for the cellular uptake studies as established before (Mehra et al., 2018). After 48 h, treated cells were washed with PBS (pH 7.4) and fixed with 4% paraformaldehyde (PFA) solution.

### Immunostaining of cells

p53 core fibril treatment was given to the cells as discussed above and a colocalization study was performed to analyze the state of p53 in the cells at T1 and T5 passage. Briefly, 4% PFA (Himedia, Mumbai, India) was used for fixing cells on the coverslips for 15 mins followed by washing with phosphate-buffered saline (PBS, pH=7.4). Permeabilization buffer containing 0.2% Triton X (Sigma-Aldrich, USA) in PBS was added to cells for 10 mins. The cells were then washed with PBS and incubated for 1 h with 2.5% BSA (Himedia, India) in PBS for blocking the non-specific epitopes. Next, the cells were incubated at 4°C overnight with mouse monoclonal anti-human p53 primary antibody DO-1 (1:200 dilution, cat. no. sc-126, RRID: AB\_628082, Santa Cruz Biotechnology, Inc., USA) and rabbit amyloid fibril-specific OC antibody (1:500 dilution, ab201062, Abcam, UK). After incubation, cells were washed three times with 0.1% Tween 20 in PBS (PBST). The coverslips were incubated for 2 h with goat anti-mouse-IgG conjugated to FITC (against p53) and goat anti-rabbit-IgG conjugated to Alexa Fluor 555 (against OC) (Cat# A27039, RRID: AB\_2536100, Invitrogen, USA) at 1:500 dilution. Cells were rinsed three times with PBST, pH 7.4. Mounting medium with DABCO (1%, Sigma-Aldrich), 90% glycerol and 10% PBS was used for preserving the coverslips. Imaging was undertaken using the Zeiss Observer Z1 microscope (Zeiss, Germany) fitted with a high-speed microlens-enhanced Nipkow spinning disc. Immunostaining for Ki-67 (Cat# sc-23900, RRID: D1819, Santa Cruz Biotechnology, Inc., USA) was carried out as mentioned above with 1:500 primary antibody and 1:1000 anti-mouse-IgG secondary antibody. Immunostaining for Pab240 (Cat# sc-99, RRID: K2020, Santa Cruz Biotechnology, Inc., USA) was carried out as mentioned above with 1:500 primary antibody and 1:1000 anti-mouse-IgG secondary antibody.

### Separation of the soluble and insoluble fraction of p53

p53 core fibril treatment was given to the MCF 10A cells and cells were passaged as discussed above along with the untreated cells. The cells were trypsinized and pelleted at 800 *g* for 15 min. The pellet was homogenized in ice-cold RIPA lysis buffer (Sigma-Aldrich, USA) on ice and centrifuged at 1000 *g* for 15 min. The supernatant including the soluble protein fraction was removed. The pellet containing the insoluble fraction was further extracted using 5% SDS as a detergent to ensure cell lysis. The protein concentration of soluble and insoluble fractions was measured using the Bradford protein estimation method. An equal amount of both fractions (50 µg) was loaded on 15% SDS-PAGE gels and subjected to western blot analysis. The membrane was rinsed with Tris-buffered saline (TBS) followed by blocking with 5% skimmed milk powder (dissolved in TBS) for 2 h at room temperature on a rocker. The membrane was incubated with mouse monoclonal anti-human p53 primary antibody DO-1 (1:500 dilution, Cat# sc-126, RRID: AB\_628082, Santa Cruz Biotechnology, Inc., USA), overnight at 4°C. The blots were washed three times (10 min each wash) with TBST (0.1% Tween 20). Secondary immunoblotting was done using goat anti-mouse-IgG secondary antibody conjugated to horseradish peroxidase (Calbiochem, USA, #401253) (1:5000 dilution in 2% BSA in TBS) for 2 h at room temperature with constant rocking. Next, three washes (10 min each) were given with TBST (0.1% Tween 20) and the blot was treated with Clarity Western ECL Substrate (Bio-Rad, USA, #1705060) and visualized by ImageQuant LAS 500 chemiluminescence CCD camera (Cytiva, USA).

### FACS for evaluating cell viability

MCF 10A cells were seeded at a density of 10<sup>4</sup> cells per well and incubated for 48 h in a 5% CO<sub>2</sub> incubator at 37°C. These cells were then treated with fibrils as mentioned above. The cells were passaged as stated. The cells at T1 and T5 passages were evaluated for cell viability. For that, cells were trypsinized and stained using an Annexin V-FITC/PI apoptosis assay kit

according to the manufacturer's protocol (BD Pharmingen FITC Annexin V Apoptosis Detection Kit I, cat# 556547). For quantifying the apoptotic population, FACS analysis was done in the BD FACS Aria Fusion SORP instrument (BD Biosciences, USA).

For the CDK1 knockdown study, cells were treated with fibrils as mentioned above, transfected with siRNA against CDK1 (see below), followed by actinomycin D treatment (ActD, Sigma-Aldrich). For this, 2  $\mu\text{g/ml}$  ActD was added for another 6 h to induce apoptotic stress before evaluating the cell viability;  $n=3$  independent experiments were done in each case.

### Soft agar colony formation assay

A soft agar colony formation assay was performed to evaluate the transformative potential of core fibril-treated MCF 10A cells at T1 and T5 passages. Corresponding untreated cells were passaged and analyzed as controls. For the assay, cell culture medium ( $2\times$ ) was prepared by dissolving DMEM powder (1 g, Gibco, USA) and sodium bicarbonate (0.2 g, Himedia, India) in 50 ml autoclaved deionized water and sterilized using a 0.22  $\mu\text{m}$  filter. 1.8 g of noble agar was added to 100 ml of distilled water to make 1.8% agarose. This stock of agarose was diluted to 0.3% and 0.6% using  $2\times$  DMEM for making the bottom and top layers, respectively, in the 12-well plate. First, the wells were covered with a 0.3% agarose mixture (bottom layer) and the agarose was solidified for 30 min at room temperature. Second, for the upper layer, untreated and treated cells were pelleted at 200  $g$  for 3 min. The cells were resuspended in assay medium and viability was counted.  $10^6$  cells per well were mixed with melted 0.6% agarose solution at 42°C. The agarose suspension with cells was then added as a top layer to the wells. The agarose suspension with cells was allowed to solidify and then placed into a 37°C incubator. The plates were observed, imaged and counted using a bright-field microscope Leica DMi1 (Leica, Germany). Normalization was done by calculating the ratio of core-treated cells at T1 or T5 passage to untreated cells at corresponding passage (T1 or T5). Three independent experiments were undertaken ( $n=3$ ). Similarly, Saos-2 cells were used for soft agar colony formation assay at T1 passage after fibril treatment ( $n=3$ ).

### Senescence-associated $\beta$ -galactosidase staining

MCF 10A cells were treated with p53 core fibrils for 48 h and passaged, as were untreated control cells. The percentage of senescent cells was evaluated at T1 and T5 generations. Cells were washed twice with PBS (500  $\mu\text{l}$  per well), and 250  $\mu\text{l}$  of 4% PFA solution was used to fix the cells for 5 min at room temperature. SA- $\beta$ -gal staining was performed according to the conventional protocol (Gary and Kindell, 2005). For this, SA- $\beta$ -gal staining solution (pH 6.0) was prepared by mixing 0.1% X-gal (Thermo Fisher Scientific), 5 mM potassium ferrocyanide, 5 mM potassium ferricyanide, 150 mM sodium chloride and 2 mM magnesium chloride in 40 mM citric acid/sodium phosphate solution. The wells containing fixed cells were treated with SA- $\beta$ -gal solution (250  $\mu\text{l}$ ) and plate was incubated in the dark at 37°C. After 72 h, the staining solution was removed and cells were washed with distilled water. The chromogenic substrate X-Gal in staining solution is cleaved in senescent cells containing galactosidase enzyme to develop a blue precipitate, staining the senescent cells blue. Cells were imaged using a  $10\times$  objective under inverted bright-field Leica DMi1 microscope (Leica, Germany) and blue-stained cells were counted. The percentage of SA- $\beta$ -gal positive cells from the total cells ( $n>200$ ) was calculated over three independent experiments.

### Microarray analysis

MCF 10A cells were treated with core fibril seeds along with untreated controls and were cultured until the T5 generation as described above. RNA isolation was performed for T1 and T5 generation for fibril-treated and untreated cells using the RNeasy mini kit (Qiagen, Germany) as per the manufacturer's protocol. The purity/concentration of the RNA was evaluated using the Nanodrop Spectrophotometer (Thermo Fisher Scientific; 2000). The integrity of the RNA was analyzed on the Bioanalyzer (Agilent; 2100 expert). Microarray analysis (outsourced) was undertaken by using RNA isolated from the early (T1) and late (T5) passage after treatment. The microarray hybridization and scanning were performed at the Agilent certified microarray facility of Genotypic Technology,

Bengaluru, India. The samples for gene expression were labeled using the Agilent Quick-Amp labeling kit (p/n5190-0442). The total RNA was reverse transcribed at 40°C using an oligo(dT) primer with a T7 polymerase promoter and converted into double-stranded cDNA, which was further used as a template for cRNA generation. cRNA was generated by *in vitro* transcription and the dye Cy3 CTP (Agilent) was incorporated during this step. The cDNA synthesis and *in vitro* transcription steps were carried out at 40°C. Labeled cRNA was cleaned up using Qiagen RNeasy columns (Qiagen, Cat No: 74106) and verified using the Nanodrop ND-1000. Labeled cRNA samples were fragmented at 60°C and hybridized on an Agilent Human Gene Expression Microarray 8X60K. Fragmentation of labeled cRNA and hybridization were undertaken using the Gene Expression Hybridization kit of Agilent Technologies (*In situ* Hybridization kit, Part Number 5190-0404). Hybridization was carried out in Agilent's Surehyb Chambers at 65°C for 16 h. The hybridized slides were washed using Agilent Gene Expression wash buffers (Agilent Technologies, Part Number 5188-5327) and scanned using the Agilent Microarray Scanner (Agilent Technologies Part Number G2600D). Raw data extraction from images was obtained using Agilent Feature Extraction software and analyzed using Agilent GeneSpring GX (v14.5) software. Normalization of the data was undertaken in GeneSpring GX using the 75th percentile shift method (percentile shift normalization is a global normalization, where the locations of all the spot intensities in an array are adjusted). This normalization takes each column in an experiment independently, and computes the percentile of the expression values for this array, across all spots (where  $n$  has a range from 0–100 and  $n=75$  is the median). It subtracts this value from the expression value of each entity and fold change values were obtained by comparing test samples with respect to specific control samples. Significant genes upregulated with fold change  $\geq 1$  (logbase2) and down-regulated with fold change  $\leq -1$  (logbase2) in the test samples with respect to the control sample were identified.  $P$ -values were calculated using Benjamini-Hochberg correction for multiple hypothesis testing to calculate the false discovery rate (FDR). Genes with more than 2-fold change in gene expression and an adjusted  $P$ -value (FDR)  $< 0.05$  were classified as differentially expressed and used for further analysis. Differentially regulated genes were processed by hierarchical clustering based on the Pearson coefficient correlation algorithm to identify significant gene expression patterns. The biological analysis was done for the differentially expressed genes based on their functional category and pathways using Metascape (Zhou et al., 2019b) (<http://metascape.org/>). The microarray dataset is available at NCBI Gene Expression Omnibus (accession number GSE150522).

### Quantitative real-time PCR

MCF 10A cells were treated with core fibril seeds and cultured until the T5 generation as described above. At each generation (T1 to T5), the cell pellet was collected for RNA isolation. RNA isolation was undertaken from the treated cells and untreated cells using the TriZol (Invitrogen) method according to the manufacturer's protocol. Briefly, the cell pellet was lysed using 700  $\mu\text{l}$  of TriZol for a single 12-well plate. Next, 400  $\mu\text{l}$  of chloroform was added and samples were vortexed vigorously. Samples were centrifuged at 12,000  $g$  for 15 min at 4°C. The aqueous phase (upper layer) was transferred to fresh tubes and an equal volume of isopropyl alcohol was added for precipitation of RNA. Samples were kept at room temperature for 20 mins and centrifuged at 12,000  $g$  for 10 min at 4°C. The supernatant was removed carefully and the RNA pellet was washed using 70% ethanol followed by centrifugation at 7500  $g$  for 5 min at 4°C. Ethanol was allowed to evaporate and RNA was resuspended in nuclease-free water. A Nanodrop spectrophotometer (Implen, USA) was used to measure the concentration of the isolated RNA. cDNA synthesis was done with RevertAid first-strand cDNA synthesis kit with random hexamer primers (Thermo Fisher Scientific) according to the manufacturer's protocol. Quantitative real-time PCR (qRT-PCR) was performed using the SYBR Green method using primers for p21 (*CDKN1A*), *BAX*, *DDB2*, *CCND2* and *MAPK1* genes (refer to Table S1 for primer sequences). Maxima SYBR Green/ROX qPCR Master Mix ( $2\times$ ) (Thermo Fisher Scientific) was used according to the manufacturer's protocol. The amplification of target gene cDNAs was quantified by measuring the threshold ( $C_t$ ) values. To determine the relative

expression, all the data were normalized to the expression of housekeeping gene (GAPDH) and then the fold changes ( $2^{-\Delta\Delta Ct}$ ) were calculated compared to the controls.  $n=2$  independent experiments.

### Comparison of pathways in cells with mutant p53 and amyloid p53

We used single-sample gene set enrichment analysis (ssGSEA), to compute activity scores on Hallmark signatures obtained from MSigDB (Liberzon et al., 2015). For comparison of p53 amyloid to p53 mutants, we used the datasets GSE150522 (WT p53 MCF 10A and p53 amyloid treated MCF 10A cells) and GSE75168 (WT p53 MCF 10A cells and p53 mutant MDA-MB-231 cells). MDA-MB-231 and MDA-MB-468 cells from datasets in GSE14491, GSE26262, GSE53153 and GSE68249 were considered as proxies for p53 contact mutations. Similarly, BT549, SUM149 and HCC1395 from GSE68249 were considered as proxies for structural p53 mutants. All the mutant datasets were obtained from published literature (Adorno et al., 2009; Di Minin et al., 2014; Freed-Pastor et al., 2012; Girardini et al., 2011; Walerych et al., 2016). A pathway was considered dysregulated if it had a  $P<0.01$  from an unpaired two-tailed Student's  $t$ -test under the assumption of unequal variances upon comparison with the corresponding control case.

### Sample preparation for proteomics analysis

Proteomic analysis was carried out using iTRAQ labeling coupled with LC-MS/MS (Datta et al., 2017; Zhao et al., 2016). For this, MCF 10A cells were treated with core fibril seeds and cultured until the T5 generation as described above. The cells without core fibril treatment were used as control. Cells at T1 and T5 passages were pelleted down at 4°C. Proteins were extracted from the harvested cell pellet by RIPA lysis and extraction buffer (Sigma-Aldrich; 150 mM NaCl, 1.0% IGEPAL® CA-630, 0.5% sodium deoxycholate, 0.1% SDS, 50 mM Tris-HCl pH 8.0) containing protease and phosphatase inhibitor cocktail (Thermo Fisher Scientific, USA) with intermediate vortexing, followed by mild sonication. The lysate was centrifuged at 14,000  $g$  for 30 min at 4°C. The supernatant was collected and acetone precipitation of the proteins was performed at  $-20^{\circ}\text{C}$ . The protein precipitates were re-solubilized in 8 M urea. The protein concentration was estimated with the BCA protein assay kit (Thermo Fisher Scientific).

### iTRAQ labeling and fractionation by reverse phase chromatography

From each sample, an equal amount of protein (40  $\mu\text{g}$ ) was incubated with 5 mM DTT (37°C, 60 min) for reduction and alkylated with 20 mM iodoacetamide (IAA) (room temperature, 30 min, dark). MS grade trypsin (Pierce, Thermo Fisher Scientific) was added to convert the proteins into peptides [trypsin; protein ratio of 1:20 (w/w) at pH 8, 37°C for 24 h]. 1% formic acid was added to lower the pH and to quench the activity of trypsin. Next, the peptides obtained were labeled with isobaric mass tags (iTRAQ labeling) using the iTRAQ Reagent 8-Plex kit (SCIEX, USA) based on the manufacturer's protocol. In the T1 generation, the samples were labeled with isobaric mass tags as follows: control (untreated) samples with mass tags 113 and 115, P8 peptide-treated (Ghosh et al., 2017) samples with mass tag 114 (data not shown) and core fibril-treated samples with mass tag 116. Similarly, in the T5 generation the samples were labeled as follows: control (untreated) samples with mass tags 117 and 119, P8 peptide-treated samples (data not shown) with mass tag 118 and core fibril-treated samples with mass tag 121. The samples were incubated at room temperature for 2 h before pooling them together. Two biological repeats were carried out. To reduce the proteome complexity, basic reverse phase chromatography (BRP) was performed using 1260 Infinity HPLC system (Agilent, USA). A total of 320  $\mu\text{g}$  combined labeled peptides were loaded onto the C18 column (Agilent, USA, 300 extend-C18; 3.5  $\mu\text{m}$ ; 2.1 $\times$ 150 mm) which was previously equilibrated with solvent A (10 mM ammonium formate, pH 10) and the column temperature was maintained at 40°C. A gradient from 2–50% of solvent B (10 mM ammonium formate in 90% acetonitrile, pH 10) over 65 min total run at a flow rate of 0.5 ml/min was used for elution of peptides. The eluted fractions were pooled to 10 fractions for each biological replicate, vacuum dried, desalted with C18 tips (Pierce, USA), and

reconstituted with solvent C [2% (v/v) acetonitrile, 0.1% (v/v) formic acid in water] for LC-MS/MS analysis.

### LC-MS/MS acquisition

All HPLC purified fractions were analyzed in Sciex 5600+ Triple-TOF mass spectrometer coupled with ChromXP reversed-phase 3  $\mu\text{m}$  C18-CL trap column (350  $\mu\text{m}\times$ 0.5 mm, 120 Å, Eksigent) and nanoViper C18 separation column (75  $\mu\text{m}\times$ 250 mm, 3  $\mu\text{m}$ , 100 Å; Acclaim Pep Map, Thermo Fisher Scientific) in Eksigent nanoLC (Ultra 2D plus) system. The binary mobile solvent system was used as follows: solvent C [2% (v/v) acetonitrile, 0.1% (v/v) formic acid in water] and solvent D [98% (v/v) acetonitrile, 0.1% (v/v) formic acid]. The peptides were separated using a 70 min gradient from 5–50% of solvent D at a flow rate of 200 nl/min. The MS data of each fraction was acquired in information-dependent acquisition (IDA) with high sensitivity mode. The collision energy was set to iTRAQ reagent. Each cycle consisted of 250 and 100 ms acquisition time for MS1 ( $m/z$  400–1250 Da) and MS/MS (70–1800  $m/z$ ) scans, respectively, with a total cycle time of 2.3 s. Each fraction was run in duplicate.

### Peptide and protein identification

All raw files (.wiff) were converted to the Mascot generic file (mgf) format using Peak View (version 1.2.0.3). ProteinPilot software (version 4.5, SCIEX) with the Paragon algorithm was used for protein identification and relative iTRAQ quantification. Proteins were identified against the UniProt human-reviewed database containing only canonical sequences (downloaded in April 2020). The search parameters were set as follows: iTRAQ 8plex (peptide labeled); IAA Cysteine alkylation; digestion enzyme Trypsin. Peptides and proteins were validated at  $<1\%$  false discovery rate (FDR) and with unused score  $>1.3$  (which corresponds to  $>95\%$  confidence). The cutoff value for upregulation and downregulation of proteins was set to  $>1.3$  and  $<0.8$ , respectively, with  $P<0.05$ . The fold change was presented as the relative expression ratio of a given protein in the core fibril seed-treated cells to that in the untreated control. The differential abundance of proteins from two biological replicates was combined and used further for downstream analysis. The mass spectrometry proteomics data has been deposited to the ProteomeXchange Consortium via the PRIDE partner repository with the dataset identifier PXD019498.

### Ontology analysis – pathways and functional enrichment

The list of differentially expressed (the ratio threshold  $>1.3$  or  $<0.80$ ,  $P<0.05$ ) proteins was extracted with SwissProt accession. The web server-based software WEB-based Gene Set AnaLysis Toolkit (Zhang et al., 2005) (<http://webgestalt.org>) and NetworkAnalyst 3.0 (Zhou et al., 2019a) were used with their default settings for functional enrichment and annotation. An overrepresentation enrichment analysis (ORA) was performed in WebGestalt for gene ontology (GO) analysis using a non-redundant functional database. The Reactome database was used for pathway analysis. Signaling networks were built by using NetworkAnalyst 3.0 using the STRING interactome database (Szklarczyk et al., 2019). The mass spectrometry proteomics data are available via ProteomeXchange dataset identifier PXD019498.

### MTT assay

An 3-[4,5-dimethylthiazol-2-yl]-2,5 diphenyl tetrazolium bromide (MTT) assay to estimate the survival of the MCF 10A cells (fibril-treated and untreated at T1 and T5 generation) was carried out with various inhibitors. The compounds flavopiridol hydrochloride hydrate and PD 98059 (Sigma-Aldrich) were dissolved in DMSO to make a stock concentration of 1 mM and further dilutions were made in sterile PBS (pH=7.4). MCF 10A cells at T1 and T5 (untreated and core fibril-treated) or MCF 7 cells were independently seeded ( $10^4$  cells per well) and incubated overnight. 100  $\mu\text{l}$  of DMEM containing the compounds of increasing concentration (0, 0.5, 1 and 5  $\mu\text{M}$  for flavopiridol; 0–100  $\mu\text{M}$  for PD 98059) was added to the wells. The samples were analyzed in triplicates. PBS buffer, 0.1% DMSO (negative control) and 10% Triton-X (positive control) were used. The medium with cells (normalized to 100% viability at each passage) and cell-free medium alone (for background absorbance) were used and the plate was incubated for 24 h. Then 10  $\mu\text{l}$  of MTT dye (Sigma-Aldrich; 5 mg/ml) in PBS was

added to the wells for 4 h followed by overnight lysis using addition of 100  $\mu$ l of DMF-SDS (50% N,N dimethylformamide and 20% SDS). Measurement was performed in a SpectraMax M2<sup>®</sup> (Molecular Devices) plate reader. The background scattering at 690 nm was subtracted from the absorbance values at 560 nm. The percentage viability of cells was calculated as (absorbance of sample–absorbance of blank/absorbance of control–absorbance of blank)×100. EC<sub>50</sub> values for flavopiridol and PD98059 were calculated using GraphPad Prism software.

### siRNA-mediated knockdown of CDK1

MCF 10A cells were seeded in 24- or 96-well plates to reach ~80% confluency in 24 h. The cells were then treated with p53 core fibril seeds as described above. The cells were preincubated with Opti-MEM for at least 6 h for the siRNA transfection against the CDK1 gene. Transfection was performed with Ambion Silencer pre-designed siRNA (21-nucleotide oligomer dsRNA, Thermo Fisher Scientific, #103821) using Lipofectamine<sup>™</sup> RNA iMAX Transfection Reagent (Invitrogen, USA, #13778075) as per the manufacturer's protocol. 30 nM siRNA was used to knock down the expression of CDK1. As a control, Silencer<sup>™</sup> Negative Control No. 1 siRNA (Ambion #AM4611) was used (control dsRNA). Refer to Table S1 for siRNA sequences. The medium from the wells was replaced with MCF 10A assay medium after 8 h. Cells were harvested for the western blot analysis of CDK1 levels after 48 h of transfection, thereby optimizing the concentration of siRNA required for an efficient knockdown. Subsequent knockdown experiments were performed using a 30 nM concentration of siRNA as it showed >90% knockdown of CDK1.

### Western blotting

Whole-cell lysates were prepared using RIPA buffer (ready-to-use solution, Sigma-Aldrich) containing 150 mM NaCl, 1.0% IGEPAL<sup>®</sup> CA-630, 0.5% sodium deoxycholate, 0.1% SDS, 50 mM Tris-HCl pH 8.0 (Sigma-Aldrich, #R0278). Total protein content in the lysates was measured using the Bradford assay. 30  $\mu$ g protein from each sample was mixed with sample buffer containing 5%  $\beta$ -mercaptoethanol and incubated at 100°C. Samples were resolved in 15% SDS-PAGE and proteins were transferred from gel to nitrocellulose membrane (Immobilon-NC Transfer Membrane, 0.45  $\mu$ m HATF, Merck Millipore, Germany, #HATF00010) by wet transfer method at 4°C for 2 h at a constant voltage (100 V) using Bio-Rad transfer apparatus. After transfer, the membrane was rinsed with TBS followed by blocking with 5% skimmed milk powder (dissolved in TBS) for 2 h at room temperature on a rocker. Immunoblotting on the membrane was carried out with primary mouse monoclonal antibody; anti-CDK1 (Invitrogen, USA, #33-1800; 1:500 dilution in 2% BSA dissolved in TBS) and mouse anti-GAPDH (1:2000; sc-365062, Santa Cruz Biotechnology, USA) for overnight at 4°C. The blots were washed three times (15 min each wash) with TBST (0.1% Tween 20). Secondary immunoblotting was done using goat anti-mouse-IgG secondary antibody conjugated to horseradish peroxidase (Calbiochem, USA, #401253) (1:5000 dilution in 2% BSA in TBS) for 2 h at room temperature with constant rocking. Next, three washes (15 min each) were given with TBST (0.1% Tween 20) and the blot was treated with Clarity Western ECL Substrate (Bio-Rad, USA, #1705060) and visualized by ImageQuant LAS 500 chemiluminescence ChemiDoc coupled with CCD camera (Cytiva, USA). Images were processed using Image J software for quantitative analysis. Three independent experiments were carried out.

### Statistical analysis

The statistical significance [ $*P<0.05$ ,  $**P<0.01$ ,  $***P<0.001$ , non-significant (ns,  $P>0.05$ )] was calculated by one-way ANOVA followed by a Bonferroni multiple comparison post hoc test with 95% confidence interval. KaleidaGraph, version 4.1 software was used for calculating the statistical significance. No outliers were excluded from analysis and no assessment was made for outliers and normality of data.

### Acknowledgements

We acknowledge IIT Bombay for central facilities used (FACS, TEM and confocal microscopy).

### Competing interests

The authors declare no competing or financial interests.

### Author contributions

Conceptualization: A.N., S.K.M.; Methodology: A.N., A.P., A.S., S.P., A.K.D., S. Saha; Formal analysis: A.N., A.P., S.P., S. Sahoo, M.K.J., T.K.M.; Investigation: A.N.; Writing - original draft: A.N., S.K.M.; Writing - review & editing: S.K.M.; Visualization: A.N.; Supervision: S.K.M.; Funding acquisition: S.K.M.

### Funding

The authors acknowledge Department of Science and Technology, Ministry of Science and Technology, India (DST-SERB; CRG/2019/001133), Government of India for financial support. A.N. acknowledges University Grants Commission and Council of Scientific and Industrial Research (UGC-CSIR), Government of India for the fellowship. S.P. acknowledges DST-SERB, Government of India for funding and fellowship. A.P. acknowledges Council of Scientific and Industrial Research Government of India for the Shyama Prasad Mukherjee fellowship. A.S. acknowledges Indian Institute of Technology Bombay for the Institute Post-Doctoral fellowship.

### Data availability

The microarray dataset is available to download using NCBI Gene Expression Omnibus accession number GEO accession number GSE150522. The mass spectrometry proteomics data are available via ProteomeXchange with dataset identifier PXD019498.

### Peer review history

The peer review history is available online at <https://journals.biologists.com/jcs/article-lookup/doi/10.1242/jcs.259500>.

### References

- Adorno, M., Cordenonsi, M., Montagner, M., Dupont, S., Wong, C., Hann, B., Solari, A., Bobisse, S., Rondina, M. B., Guzzardo, V. et al. (2009). A mutant-p53/Smad complex opposes p63 to empower TGF- $\beta$ -induced metastasis. *Cell* **137**, 87–98. doi:10.1016/j.cell.2009.01.039
- Alberti, S., Halfmann, R. and Lindquist, S. (2010). Biochemical, cell biological, and genetic assays to analyze amyloid and prion aggregation in yeast. *Methods Enzymol.* **470**, 709–734. doi:10.1016/S0076-6879(10)70030-6
- Alessi, D. R., Cuenda, A., Cohen, P., Dudley, D. T. and Saltiel, A. R. (1995). PD 098059 is a specific inhibitor of the activation of mitogen-activated protein kinase *in vitro* and *in vivo*. *J. Biol. Chem.* **270**, 27489–27494. doi:10.1074/jbc.270.46.27489
- Ano Bom, A. P. D., Rangel, L. P., Costa, D. C. F., de Oliveira, G. A., Sanches, D., Braga, C. A., Gava, L. M., Ramos, C. H. I., Cepeda, A. O., Stumbo, A. C. et al. (2012). Mutant p53 aggregates into prion-like amyloid oligomers and fibrils: implications for cancer. *J. Biol. Chem.* **287**, 28152–28162. doi:10.1074/jbc.M112.340638
- Bell, S., Klein, C., Müller, L., Hansen, S. and Buchner, J. (2002). p53 contains large unstructured regions in its native state. *J. Mol. Biol.* **322**, 917–927. doi:10.1016/S0022-2836(02)00848-3
- Bosari, S., Viale, G., Bossi, P., Maggioni, M., Coggi, G., Murray, J. J. and Lee, A. K. C. (1994). Cytoplasmic accumulation of p53 protein: an independent prognostic indicator in colorectal adenocarcinomas. *J. Natl. Cancer Inst.* **86**, 681–687. doi:10.1093/jnci/86.9.681
- Bosari, S., Viale, G., Roncalli, M., Graziani, D., Borsani, G., Lee, A. K. and Coggi, G. (1995). p53 gene mutations, p53 protein accumulation and compartmentalization in colorectal adenocarcinoma. *Am. J. Pathol.* **147**, 790–798.
- Boysen, M., Kityk, R. and Mayer, M. P. (2019). Hsp70- and Hsp90-mediated regulation of the conformation of p53 DNA binding domain and p53 cancer variants. *Mol. Cell* **74**, 831–843.e4. doi:10.1016/j.molcel.2019.03.032
- Brabletz, T., Kalluri, R., Nieto, M. A. and Weinberg, R. A. (2018). EMT in cancer. *Nat. Rev. Cancer* **18**, 128–134. doi:10.1038/nrc.2017.118
- Brachmann, A., Baxa, U. and Wickner, R. B. (2005). Prion generation *in vitro*: amyloid of Ure2p is infectious. *EMBO J.* **24**, 3082–3092. doi:10.1038/sj.emboj.7600772
- Carlson, B. A., Dubay, M. M., Sausville, E. A., Brizuela, L. and Worland, P. J. (1996). Flavopiridol induces G1 arrest with inhibition of cyclin-dependent kinase (CDK) 2 and CDK4 in human breast carcinoma cells. *Cancer Res.* **56**, 2973.
- Datta, A., Chai, Y. L., Tan, J. M., Lee, J. H., Francis, P. T., Chen, C. P., Sze, S. K. and Lai, M. K. P. (2017). An iTRAQ-based proteomic analysis reveals dysregulation of neocortical synaptotaxin in Lewy body dementias. *Mol. Brain* **10**, 36. doi:10.1186/s13041-017-0316-9
- De Smet, F., Saiz Rubio, M., Hompes, D., Naus, E., De Baets, G., Langenberg, T., Hipp, M. S., Houben, B., Claes, F., Charbonneau, S. et al. (2017). Nuclear inclusion bodies of mutant and wild-type p53 in cancer: a hallmark of p53 inactivation and proteostasis remodelling by p53 aggregation. *J. Pathol.* **242**, 24–38. doi:10.1002/path.4872



- Di Minin, G., Bellazzo, A., Dal Ferro, M., Chiaruttini, G., Nuzzo, S., Bicciato, S., Piazza, S., Rami, D., Bulla, R., Sommaggio, R. et al. (2014). Mutant p53 reprograms TNF signaling in cancer cells through interaction with the tumor suppressor DAB2IP. *Mol. Cell* **56**, 617–629. doi:10.1016/j.molcel.2014.10.013
- Fowler, D. M., Koulov, A. V., Balch, W. E. and Kelly, J. W. (2007). Functional amyloid—from bacteria to humans. *Trends Biochem. Sci.* **32**, 217–224. doi:10.1016/j.tibs.2007.03.003
- Freed-Pastor, W. A., Mizuno, H., Zhao, X., Langerød, A., Moon, S.-H., Rodriguez-Barrueco, R., Barsotti, A., Chicas, A., Li, W., Polotskaia, A. et al. (2012). Mutant p53 disrupts mammary tissue architecture via the mevalonate pathway. *Cell* **148**, 244–258. doi:10.1016/j.cell.2011.12.017
- Fuster, J. J., Sanz-González, S. M., Moll, U. M. and Andrés, V. (2007). Classic and novel roles of p53: prospects for anticancer therapy. *Trends Mol. Med.* **13**, 192–199. doi:10.1016/j.molmed.2007.03.002
- Gary, R. K. and Kindell, S. M. (2005). Quantitative assay of senescence-associated  $\beta$ -galactosidase activity in mammalian cell extracts. *Anal. Biochem.* **343**, 329–334. doi:10.1016/j.ab.2005.06.003
- Ghosh, D., Mondal, M., Mohite, G. M., Singh, P. K., Ranjan, P., Anoop, A., Ghosh, S., Jha, N. N., Kumar, A. and Maji, S. K. (2013). The Parkinson's disease-associated H50Q mutation accelerates  $\alpha$ -synuclein aggregation *in vitro*. *Biochemistry* **52**, 6925–6927. doi:10.1021/bi400999d
- Ghosh, S., Ghosh, D., Ranganathan, S., Anoop, A., P. S. K., Jha, N. N., Padinhateeri, R. and Maji, S. K. (2014). Investigating the Intrinsic Aggregation Potential of Evolutionarily Conserved Segments in p53. *Biochemistry* **53**, 5995–6010. doi:10.1021/bi500825d
- Ghosh, S., Salot, S., Sengupta, S., Navalkar, A., Ghosh, D., Jacob, R., Das, S., Kumar, R., Jha, N. N., Sahay, S. et al. (2017). p53 amyloid formation leading to its loss of function: implications in cancer pathogenesis. *Cell Death Differ.* **24**, 1784. doi:10.1038/cdd.2017.105
- Giancotti, F. G. (2014). Deregulation of cell signaling in cancer. *FEBS Lett.* **588**, 2558–2570. doi:10.1016/j.febslet.2014.02.005
- Girardini, J. E., Napoli, M., Piazza, S., Rustighi, A., Marotta, C., Radaelli, E., Capaci, V., Jordan, L., Quinlan, P., Thompson, A. et al. (2011). A Pin1/mutant p53 axis promotes aggressiveness in breast cancer. *Cancer Cell* **20**, 79–91. doi:10.1016/j.ccr.2011.06.004
- Halfmann, R., Jarosz, D. F., Jones, S. K., Chang, A., Lancaster, A. K. and Lindquist, S. (2012). Prions are a common mechanism for phenotypic inheritance in wild yeasts. *Nature* **482**, 363–368. doi:10.1038/nature10875
- Hanahan, D. and Weinberg, R. A. (2000). The hallmarks of cancer. *Cell* **100**, 57–70. doi:10.1016/S0092-8674(00)81683-9
- Hartl, F. U., Bracher, A. and Hayer-Hartl, M. (2011). Molecular chaperones in protein folding and proteostasis. *Nature* **475**, 324–332. doi:10.1038/nature10317
- Hsu, P. P. and Sabatini, D. M. (2008). Cancer cell metabolism: Warburg and Beyond. *Cell* **134**, 703–707. doi:10.1016/j.cell.2008.08.021
- Joerger, A. C. and Fersht, A. R. (2007). Structure–function–rescue: the diverse nature of common p53 cancer mutants. *Oncogene* **26**, 2226–2242. doi:10.1038/sj.onc.1210291
- Kayed, R., Head, E., Sarsoza, F., Saing, T., Cotman, C. W., Neuclea, M., Margol, L., Wu, J., Breydo, L., Thompson, J. L. et al. (2007). Fibril specific, conformation dependent antibodies recognize a generic epitope common to amyloid fibrils and fibrillar oligomers that is absent in prefibrillar oligomers. *Mol. Neurodegener.* **2**, 18. doi:10.1186/1750-1326-2-18.
- Kleeff, J., Kornmann, M., Sawhney, H. and Korc, M. (2000). Actinomycin D induces apoptosis and inhibits growth of pancreatic cancer cells. *Int. J. Cancer* **86**, 399–407. doi:10.1002/(SICI)1097-0215(20000501)86:3<399::AID-IJC15>3.0.CO;2-G
- Koo, E. H., Lansbury, P. T. and Kelly, J. W. (1999). Amyloid diseases: Abnormal protein aggregation in neurodegeneration. *Proc. Natl. Acad. Sci. USA* **96**, 9989–9990. doi:10.1073/pnas.96.18.9989
- Kriegenburg, F., Ellgaard, L. and Hartmann-Petersen, R. (2012). Molecular chaperones in targeting misfolded proteins for ubiquitin-dependent degradation. *FEBS J.* **279**, 532–542. doi:10.1111/j.1742-4658.2011.08456.x
- Lasagna-Reeves, C. A., Clos, A. L., Castillo-Carranza, D., Sengupta, U., Guerrero-Muñoz, M., Kelly, B., Wagner, R. and Kaye, R. (2013). Dual role of p53 amyloid formation in cancer; loss of function and gain of toxicity. *Biochem. Biophys. Res. Commun.* **430**, 963–968. doi:10.1016/j.bbrc.2012.11.130
- Liberzon, A., Birger, C., Thorvaldsdóttir, H., Ghandi, M., Mesirov, J. P. and Tamayo, P. (2015). The Molecular Signatures Database (MSigDB) hallmark gene set collection. *Cell Syst.* **1**, 417–425. doi:10.1016/j.cels.2015.12.004
- Liebman, S. W. and Chernoff, Y. O. (2012). Prions in yeast. *Genetics* **191**, 1041–1072. doi:10.1534/genetics.111.137760
- Macaluso, M., Paggi, M. G. and Giordano, A. (2003). Genetic and epigenetic alterations as hallmarks of the intricate road to cancer. *Oncogene* **22**, 6472–6478. doi:10.1038/sj.onc.1206955
- Martin, G. S. (2003). Cell signaling and cancer. *Cancer Cell* **4**, 167–174. doi:10.1016/S1535-6108(03)00216-2
- Masison, D. C. and Wickner, R. B. (1995). Prion-inducing domain of yeast Ure2p and protease resistance of Ure2p in prion-containing cells. *Science* **270**, 93–95. doi:10.1126/science.270.5233.93
- Mehra, S., Ghosh, D., Kumar, R., Mondal, M., Gadhe, L. G., Das, S., Anoop, A., Jha, N. N., Jacob, R. S., Chatterjee, D. et al. (2018). Glycosaminoglycans have variable effects on  $\alpha$ -synuclein aggregation and differentially affect the activities of the resulting amyloid fibrils. *J. Biol. Chem.* **293**, 12975–12991. doi:10.1074/jbc.RA118.004267
- Moll, U. M. and Petrenko, O. (2003). The MDM2-p53 interaction. *Mol. Cancer Res.* **1**, 1001–1008.
- Moll, U. M., Riou, G. and Levine, A. J. (1992). Two distinct mechanisms alter p53 in breast cancer: mutation and nuclear exclusion. *Proc. Natl. Acad. Sci. USA* **89**, 7262–7266. doi:10.1073/pnas.89.15.7262
- Moll, U. M., LaQuaglia, M., Bénard, J. and Riou, G. (1995). Wild-type p53 protein undergoes cytoplasmic sequestration in undifferentiated neuroblastomas but not in differentiated tumors. *Proc. Natl. Acad. Sci. USA* **92**, 4407–4411. doi:10.1073/pnas.92.10.4407
- Moll, U. M., Ostermeyer, A. G., Haladay, R., Winkfield, B., Frazier, M. and Zambetti, G. (1996). Cytoplasmic sequestration of wild-type p53 protein impairs the G1 checkpoint after DNA damage. *Mol. Cell Biol.* **16**, 1126–1137. doi:10.1128/MCB.16.3.1126
- Muller, P. A. J. and Vousden, K. H. (2013). p53 mutations in cancer. *Nat. Cell Biol.* **15**, 2–8. doi:10.1038/ncb2641
- Navalkar, A., Ghosh, S., Pandey, S., Paul, A., Datta, D. and Maji, S. K. (2020). Prion-like p53 amyloids in cancer. *Biochemistry* **59**, 146–155. doi:10.1021/acs.biochem.9b00796
- Navalkar, A., Pandey, S., Singh, N., Patel, K., Datta, D., Mohanty, B., Jadhav, S., Chaudhari, P. and Maji, S. K. (2021). Direct evidence of cellular transformation by prion-like p53 amyloid infection. *J. Cell Sci.* **134**, jcs258316. doi:10.1242/jcs.258316
- Olzsch, H., Schermann, S. M., Woerner, A. C., Pinkert, S., Hecht, M. H., Tartaglia, G. G., Vendruscolo, M., Hayer-Hartl, M., Hartl, F. U. and Vabulas, R. M. (2011). Amyloid-like aggregates sequester numerous metastable proteins with essential cellular functions. *Cell* **144**, 67–78. doi:10.1016/j.cell.2010.11.050
- Oren, M. and Rotter, V. (2010). Mutant p53 gain-of-function in cancer. *Cold Spring Harb. Perspect. Biol.* **2**, a001107. doi:10.1101/cshperspect.a001107
- Ostermeyer, A. G., Runko, E., Winkfield, B., Ahn, B. and Moll, U. M. (1996). Cytoplasmically sequestered wild-type p53 protein in neuroblastoma is relocated to the nucleus by a C-terminal peptide. *Proc. Natl. Acad. Sci. USA* **93**, 15190–15194. doi:10.1073/pnas.93.26.15190
- Palanikumar, L., Karpauskaite, L., Al-Sayegh, M., Chehade, I., Alam, M., Hassan, S., Maity, D., Ali, L., Kalmouni, M., Hunashal, Y. et al. (2021). Protein mimetic amyloid inhibitor potentially abrogates cancer-associated mutant p53 aggregation and restores tumor suppressor function. *Nat. Commun.* **12**, 3962. doi:10.1038/s41467-021-23985-1
- Parrales, A., Ranjan, A., Iyer, S. V., Padhye, S., Weir, S. J., Roy, A. and Iwakuma, T. (2016). DNAJA1 controls the fate of misfolded mutant p53 through the mevalonate pathway. *Nat. Cell Biol.* **18**, 1233–1243. doi:10.1038/ncb3427
- Rangel, L. P., Costa, D. C. F., Vieira, T. C. R. G. and Silva, J. L. (2014). The aggregation of mutant p53 produces prion-like properties in cancer. *Prion* **8**, 75–84. doi:10.4161/pri.27776
- Rangel, L. P., Ferretti, G. D. S., Costa, C. L., Andrade, S. M. M. V., Carvalho, R. S., Costa, D. C. F. and Silva, J. L. (2019). p53 reactivation with induction of massive apoptosis-1 (PRIMA-1) inhibits amyloid aggregation of mutant p53 in cancer cells. *J. Biol. Chem.* **294**, 3670–3682. doi:10.1074/jbc.RA118.004671
- Serio, T. R. and Lindquist, S. L. (2001). The yeast prion [PSI<sup>+</sup>]: molecular insights and functional consequences. *Adv. Protein Chem.* **59**, 391–412. doi:10.1016/S0065-3233(01)59012-9
- Sever, R. and Brugge, J. S. (2015). Signal transduction in cancer. *Cold Spring Harb. Perspect. Med.* **5**, a006098. doi:10.1101/cshperspect.a006098
- Silva, J. L., Gallo, C. V. D. M., Costa, D. C. F. and Rangel, L. P. (2014). Prion-like aggregation of mutant p53 in cancer. *Trends Biochem. Sci.* **39**, 260–267. doi:10.1016/j.tibs.2014.04.001
- Silva, J. L., Cino, E. A., Soares, I. N., Ferreira, V. F. and A. P. de Oliveira, G. (2018). Targeting the prion-like aggregation of mutant p53 to combat cancer. *Acc. Chem. Res.* **51**, 181–190. doi:10.1021/acs.accounts.7b00473
- Singh, P. K., Kotia, V., Ghosh, D., Mohite, G. M., Kumar, A. and Maji, S. K. (2013). Curcumin modulates  $\alpha$ -synuclein aggregation and toxicity. *ACS Chem. Neurosci.* **4**, 393–407. doi:10.1021/cn3001203
- Soragni, A., Janzen, D. M., Johnson, L. M., Lindgren, A. G., Thai-Quynh Nguyen, A., Tiourin, E., Soriaga, A. B., Lu, J., Jiang, L., Faull, K. F. et al. (2016). A designed inhibitor of p53 aggregation rescues p53 tumor suppression in ovarian carcinomas. *Cancer Cell* **29**, 90–103. doi:10.1016/j.ccell.2015.12.002
- Stein, Y., Rotter, V. and Aloni-Grinstein, R. (2019). Gain-of-function mutant p53: all the roads lead to tumorigenesis. *Int. J. Mol. Sci.* **20**, 6197. doi:10.3390/ijms20246197
- Szklarczyk, D., Gable, A. L., Lyon, D., Junge, A., Wyder, S., Huerta-Cepas, J., Simonovic, M., Doncheva, N. T., Morris, J. H., Bork, P. et al. (2019). STRING v11: protein–protein association networks with increased coverage, supporting functional discovery in genome-wide experimental datasets. *Nucleic Acids Res.* **47**, D607–D613. doi:10.1093/nar/gky1131

- Volles, M. J. and Lansbury, P. T. Jr.** (2007). Relationships between the sequence of alpha-synuclein and its membrane affinity, fibrillization propensity, and yeast toxicity. *J. Mol. Biol.* **366**, 1510-1522. doi:10.1016/j.jmb.2006.12.044
- Walerych, D., Lisek, K., Sommaggio, R., Piazza, S., Ciani, Y., Dalla, E., Rajkowska, K., Gaweda-Walerych, K., Ingallina, E., Tonelli, C. et al.** (2016). Proteasome machinery is instrumental in a common gain-of-function program of the p53 missense mutants in cancer. *Nat. Cell Biol.* **18**, 897-909. doi:10.1038/ncb3380
- Wang, G. Z. and Fersht, A. R.** (2012). First-order rate-determining aggregation mechanism of p53 and its implications. *Proc. Natl. Acad. Sci. USA* **109**, 13590-13595. doi:10.1073/pnas.1211557109
- Wang, G. Z. and Fersht, A. R.** (2015). Mechanism of initiation of aggregation of p53 revealed by  $\Phi$ -value analysis. *Proc. Natl. Acad. Sci. USA* **112**, 2437-2442. doi:10.1073/pnas.1500243112
- Wang, G. and Fersht, A. R.** (2017). Multisite aggregation of p53 and implications for drug rescue. *Proc. Natl. Acad. Sci. USA* **114**, E2634-E2643. doi:10.1073/pnas.1700308114
- Weinstein, I. B. and Joe, A.** (2008). Oncogene addiction. *Cancer Res.* **68**, 3077. doi:10.1158/0008-5472.CAN-07-3293
- Weisz, L., Oren, M. and Rotter, V.** (2007). Transcription regulation by mutant p53. *Oncogene* **26**, 2202-2211. doi:10.1038/sj.onc.1210294
- Wickner, R. B., Taylor, K. L., Edskes, H. K., Maddelein, M.-L., Moriyama, H. and Roberts, B. T.** (2000). Prions of yeast as heritable amyloidoses. *J. Struct. Biol.* **130**, 310-322. doi:10.1006/jsbi.2000.4250
- Wickner, R. B., Edskes, H. K., Roberts, B. T., Baxa, U., Pierce, M. M., Ross, E. D. and Brachmann, A.** (2004). Prions: proteins as genes and infectious entities. *Genes Dev.* **18**, 470-485. doi:10.1101/gad.1177104
- Wickner, R. B., Shewmaker, F. P., Bateman, D. A., Edskes, H. K., Gorkovskiy, A., Dayani, Y. and Bezsonov, E. E.** (2015). Yeast prions: structure, biology, and prion-handling systems. *Microbiol. Mol. Biol. Rev.* **79**, 1-17. doi:10.1128/MMBR.00041-14
- Wilcken, R., Wang, G. Z., Boeckler, F. M. and Fersht, A. R.** (2012). Kinetic mechanism of p53 oncogenic mutant aggregation and its inhibition. *Proc. Natl. Acad. Sci. USA* **109**, 13584-13589. doi:10.1073/pnas.1211550109
- Xu, J., Reumers, J., Couceiro, J. R., De Smet, F., Gallardo, R., Rudyak, S., Cornelis, A., Rozenski, J., Zwolinska, A., Marine, J.-C. et al.** (2011). Gain of function of mutant p53 by coaggregation with multiple tumor suppressors. *Nat. Chem. Biol.* **7**, 285-295. doi:10.1038/nchembio.546
- Zhang, B., Kirov, S. and Snoddy, J.** (2005). WebGestalt: an integrated system for exploring gene sets in various biological contexts. *Nucleic Acids Res.* **33**, W741-W748. doi:10.1093/nar/gki475
- Zhao, W., Liu, Z., Yu, X., Lai, L., Li, H., Liu, Z., Li, L., Jiang, S., Xia, Z. and Xu, S.-Y.** (2016). iTRAQ proteomics analysis reveals that PI3K is highly associated with bupivacaine-induced neurotoxicity pathways. *Proteomics* **16**, 564-575. doi:10.1002/pmic.201500202
- Zhao, Y., Ge, C.-C., Wang, J., Wu, X.-X., Li, X.-M., Li, W., Wang, S.-S., Liu, T., Hou, J.-Z., Sun, H. et al.** (2017). MEK inhibitor, PD98059, promotes breast cancer cell migration by inducing  $\beta$ -catenin nuclear accumulation. *Oncol. Rep.* **38**, 3055-3063. doi:10.3892/or.2017.5955
- Zhou, G., Soufan, O., Ewald, J., Hancock, R. E. W., Basu, N. and Xia, J.** (2019a). NetworkAnalyst 3.0: a visual analytics platform for comprehensive gene expression profiling and meta-analysis. *Nucleic Acids Res.* **47**, W234-W241. doi:10.1093/nar/gkz240
- Zhou, Y., Zhou, B., Pache, L., Chang, M., Khodabakhshi, A. H., Tanaseichuk, O., Benner, C. and Chanda, S. K.** (2019b). Metascape provides a biologist-oriented resource for the analysis of systems-level datasets. *Nat. Commun.* **10**, 1523. doi:10.1038/s41467-019-09234-6
- Zilfou, J. T. and Lowe, S. W.** (2009). Tumor suppressive functions of p53. *Cold Spring Harb. Perspect. Biol.* **1**, a001883. doi:10.1101/cshperspect.a001883